University of Wisconsin Milwaukee
UWM Digital Commons

Theses and Dissertations

May 2013

Multimessenger Approach to Search for Cosmic Ray Anisotropies

Larry David Buroker
University of Wisconsin-Milwaukee

MULTIMESSENGER APPROACH TO SEARCH FOR COSMIC RAY ANISOTROPIES

By

Larry Buroker

A Thesis Submitted in

Partial Fulfillment of the

Requirements for the degree of

Master of Science

in

Physics

at

The University of Wisconsin–Milwaukee

May 2013

ABSTRACT

MULTIMESSENGER APPROACH TO SEARCH FOR COSMIC RAY ANISOTROPIES

By

Larry Buroker

The University of Wisconsin–Milwaukee, 2013
Under the Supervision of Professor Luis Anchordoqui

The origin of the highest energy cosmic rays is still unknown. The discovery of their sources will reveal the workings of the most energetic astrophysical accelerators in the universe. Recent international efforts have brought us closer to unveiling this mystery. Possible ultra-high energy cosmic ray sources have been narrowed down with the confirmation of an "ankle" and the GZK-like spectral feature at the high-end of the energy spectrum. A clear resolution of the ultra-high energy mystery calls for the search of anisotropies in the distribution of arrival directions of cosmic rays. In this thesis, we adopt the so-called "multi-messenger" approach to search for both large-scale and point-like source anisotropic features, using data collected with the Pierre Auger Observatory.

TABLE OF CONTENTS

www.manaraa.com

LIST OF FIGURES

LIST OF TABLES

ACKNOWLEDGMENTS

I would like to thank the Physics Department at the University of Wisconsin-Milwaukee for providing an excellent program and superb environment in which to learn and conduct research. It is because of this department that I was fortunate enough to have been introduced (through my advisor) to the Pierre Auger Collaboration. I am truly thankful to them for letting me work with their researchers and gain invaluable research experience from this amazing and incredible observatory. My graduate studies, culminated by this thesis, would surely not have been possible without this group and facility.

I am thankful for many professors and staff, but in particular, I wish to express my gratitude to: my advisor, Professor Luis Anchordoqui – for his guidance, motivation and optimism; Professors Jolien Creighton and Xavier Siemens for their willingness to be a part of my thesis defense committee; Jean Creighton and the Manfred Olson Planetarium for introducing me to some of the amazing things going on in modern astronomy along with letting me share some of that with others; and to Professor Prasenjit Guptasarma, Dr. Somaditya Sen, and Dr. Shishir Ray for introducing me to the research lifestyle (and also for their constant encouragement). I am extremely grateful to Ms. Kate Valerius, Physics Graduate Program Assistant, for her time and for her unending patience and for keeping me on track.

Finally, I would like to thank my friends and family who have also shown an inexhaustible amount of forbearance and encouragement throughout my studies, research and writing.

PREFACE

This thesis is based on work done with the Pierre Auger Collaboration during my graduate studies.

The Search for large-scale anisotropies (Chapter 3) is based on material from:

- Pierre Auger Collaboration

  Constraints on the origin of cosmic rays above 10^{18} *eV from large scale anisotropy searches in data of the Pierre Auger Observatory*, ApJL, 762, L **13** (2012) [arXiv:1212.3083 [astro-ph.HE]].

- Pierre Auger Collaboration

  Large scale distribution of arrival directions of cosmic rays detected above 10^{18} *eV at the Pierre Auger Observatory*, Astrophys. J. Suppl. **203**, 34 (2012) [arXiv:1210.3736 [astro-ph.HE]].

The search for sources of cosmic neutrons (Chapter 4) is based on the following paper:

- Pierre Auger Collaboration

  A Search for Point Sources of EeV Neutrons, Astrophys. J. **760**, 148 (2012) [arXiv:1211.4901 [astro-ph.HE]].

The search for sources of cosmic neutrinos (Chapter 5) is based on:

- Pierre Auger Collaboration

  Search for point-like sources of ultra-high energy neutrinos at the Pierre Auger Observatory and improved limit on the diffuse flux of tau neutrinos, Astrophys. J. **755**, L4 (2012) [arXiv:1210.3143 [astro-ph.HE]].

The following technical papers were also used in the formulation of some sections:

- Pierre Auger Collaboration

  Measurement of the Cosmic Ray Energy Spectrum Using Hybrid Events of the Pierre Auger Observatory, Eur. Phys. J. Plus **127**, 87 (2012) [arXiv:1208.6574 [astro-ph.HE]].

- Pierre Auger Collaboration

  The Rapid Atmospheric Monitoring System of the Pierre Auger Observatory, JINST **7**, P09001 (2012) [arXiv:1208.1675 [astro-ph.HE]].

- Pierre Auger Collaboration
  Antennas for the Detection of Radio Emission Pulses from Cosmic-Ray, JINST **7**, P10011 (2012) [arXiv:1209.3840 [astro-ph.IM]].

- Pierre Auger Collaboration
  Results of a self-triggered prototype system for radio-detection of extensive air showers at the Pierre Auger Observatory, JINST **7**, P11023 (2012) [arXiv:1211.0572 [astro-ph.HE]].

- Pierre Auger Collaboration
  Interpretation of the Depths of Maximum of Extensive Air Showers Measured by the Pierre Auger Observatory, JCAP **1302**, 026 (2013) [arXiv:1301.6637 [astro-ph.HE]].

- Pierre Auger Collaboration
  Techniques for Measuring Aerosol Attenuation using the Central Laser Facility at the Pierre Auger Observatory, JINST **8**, P04009 (2013) [arXiv:1303.5576 [astro-ph.IM]].

Chapter 1

Introduction

In 1909, Theodor Wulf began collecting evidence that would one day lead to the discovery of cosmic rays. Using a sealed container, he measured what seemed to be the spontaneous ionization of air. The question soon asked if this was some inherent property of the material or is the Earth itself giving off a natural radiation which was responsible for the ionization. At the time, research regarding radioactivity was still relatively young and the majority of this research centered around only three candidate processes, α-rays (ionized He), β-rays (electrons) and γ-rays. It was thought that the must be giving off γ-radiation since α and β rays were easily ruled out by shielding.

It wasn't until a few years later, in 1912, that Victor Hess (using a balloon flown at an altitude of 5 km), found that the ionization rate of air actually began to increase [1]. This clearly made no sense for radiation coming from the Earth and so Hess concluded that not only must the radiation must be coming from above, but that it must be quite powerful. Years later, in 1936, Hess would win the Nobel prize for the discovery of cosmic rays.

During this time there was much work done plotting the altitude dependence and the ionization rate of the air. Werner Kohlorster (of Germany), contributed much to this endeavor with his balloon flights as high as 9 km. These measurements, of course, came with their share of critics. One of these critics was a man named Robert Millikan, who set out to disprove the work done by Hess and Kohlorster. As fate would have it however Millikan became a major contributor to the field using methods of detection that are relatively similar to modern methods of cosmic ray detection. Using high altitude lakes, Millikan figured he could accurately determine the absorption length of cosmic rays since roughly 10 m of water corresponds to the total thickness of the atmosphere. Using this absorption length he hoped to reveal the source of cosmic rays. His thought was that cosmic rays were just high energy photons given off by the creation of new atoms. In the end his results did not help him and cosmic rays were eventually proven to be particles.

Cosmic ray research continued to move forward over the years with new detection methods including cloud chambers, nuclear emulsion stacks and Geiger counters. These new detection methods, along with advances in quantum electrodynamics and electromagnetic cascade theory as well as the advent of large particle accelerators, provided a fundamental framework upon which to build. Despite a century of advances however cosmic rays of ultra-high energies remain

something of a mystery. Specifically, it is hard to fathom the processes both in efficiency and shear energy that must be involved in accelerating these particles to energies far and beyond what is possible in our largest accelerators.

When the energies of cosmic rays cross the 10^5 GeV threshold the rate of the primaries is reduced to less than one particle per square meter per year. At this point, direct observation with a balloon, aircraft or even spacecraft becomes ineffective and only the use of ground-based observatories that have large apertures and very long exposure times are able to record a statistically significant number of cosmic ray events to be used for research. These observatories use the atmosphere itself as a sort of huge calorimeter where the incident cosmic ray primaries interact with the atomic nuclei of air molecules. The resulting air showers (or cascades) spread out over a large area.

1.1 Extensive Air Showers

The characteristics, including the size of these particle cascades, are dependent on the energy of the primary cosmic ray that initiated it and its incoming direction. In the case of ultra-high energy cosmic rays (UHECRs) showers, the cascade of secondary particles numbers in the millions and is generally hundreds of meters in diameter. The interaction of the primary cosmic rays produce pions which then decay into secondary electrons and muons which can be observed in either scintillation counters or by the Cherenkov radiation given off as these particles move through the water in tanks set up as detectors. Depending on the energy of the primary and the optimal cost-efficiency of the detector array, the detectors may be separated from 10 meters to a kilometer apart. The arrival direction can be approximately calculated by the relative arrival time and density of particles in the detector grid. The primary energy can be calibrated using the particle density in the lateral direction.

The use of fluorescence detectors is another way to measure the shower longitudinal development (or the number of particles versus the atmospheric depth), see Fig. 1. This method works by detecting the fluorescence light produced when charged particles within the atmosphere interact and produce photons. The emitted photons are generally in the ultraviolet range (300 - 400 nm), making them transparent to the atmosphere.

The invention of the coincidence circuit by Walther Bothe (1954 Nobel Prize winner) in the 1920s [3], was one of vital importance to the study of cosmic rays. The coincidence circuit generally works with one output and several inputs where the output signal is only activated when input signals arrive within a set window of time. These signals then will be considered as signals arriving at the same time. This innovation along with the advancement of fast response Geiger-Muller counters [4], led to verification that Compton scattering produced a recoiled electron as well as a γ-ray. Taking the coincidence a step further than Bothe, Bruno B. Rossi reduced the resolving time from 1.4 ms down to 0.4 ms and found accommodations for many more input channels than Bothe had used [5]. With these advances the detection of rare cosmic events became possible.
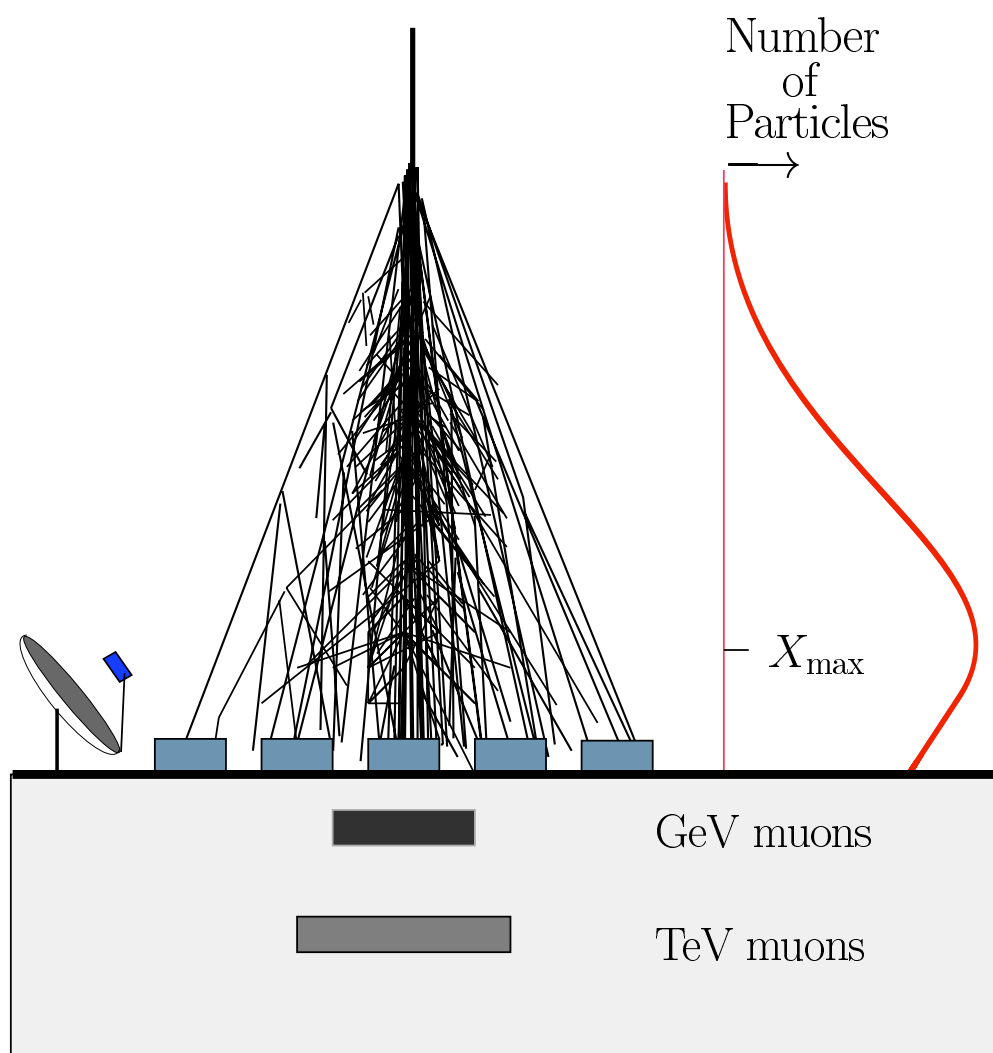
Figure 1 : Particles interacting near the top of the atmosphere initiate an electromagnetic and hadronic cascade. Its profile is shown with the red line on the right. The different detection methods are illustrated. Mirrors collect the Čerenkov and nitrogen fluorescent light, arrays of detectors sample the shower reaching the ground, and underground detectors identify the muon component of the shower [2].

The development of coincident circuits became hugely important for the discovery of extensive air showers (EAS).In 1938, Pierre Auger, found that based on the extensive size of these resulting cascades, the energy spectrum for cosmic rays must be at least 10^6 GeV and likely even greater [6, 7]. Cosmic rays of this energy and higher have an extremely low flux compared to those of lower energies, but much progress has been made in recent years with regards to measuring them. Auger and his companions observed that the chance rate expected from two counters separated by some known distance varied greatly from what was expected. Detectors, placed in the Swiss Alps, were able to be separated by up to 300 m. The observed decoherence showed the rate of pairs of coincident signals in two detectors as a function of separation and divided by the product of detector areas. In addition to detecting these EAS, Auger's group estimated that the energy of the primary was about 10^{15} eV from the number of particles in the EAS assuming each carried the critical energy, whereby particles lose energy primarily through ionization rather then bremsstrahlung radiation.

Figure 2 : Image of a particle cascade, or shower, as seen in a cloud chamber at 3027 m altitude. The primary particle is estimated to be a proton of about 10 GeV. The first interaction would most likely have been in one of the lead plates. Neutral pions feed the cascade which multiplies in the lead. Charged pions make similar interactions to protons, or decay into muons. The cross-sectional area of the cloud chamber is 0.5×0.3 m^2 and the lead absorbers have a thickness of 13 mm each [8].

With the use of cloud chambers that were triggered by Geiger counters, Auger and his collaborators were able to grasp the mechanics of air showers, at least, on a phenomenological level (see Fig. 2 for a photographic example). Although the scale is clearly different from cloud chamber images to primaries entering the atmosphere. the features of each are very similar. Early on it was know that air showers included hadronic particles, muons, and electrons and by the early 1950s the existence of pions (two charged and one neutral) led to even greater understanding of air showers.

Looking closer at Fig. 2, each lead plate is roughly two radiation lengths thick with the cross sectional area of the cloud chamber being 0.5 m x 0.3 m [8]. The radiation length is both the mean distance over which a high-energy electron loses all but 1/e of its energy by bremsstrahlung and 7/9 of the mean free path for pair productions by a high-energy photon [9]. The argon gas in the chamber between the plates was kept at atmospheric pressure, which leaves most of particle interactions, and thus shower development to happen within the plates. From the cloud chamber image we can see the sharp increase in particle count due to interactions, called the shower size. We can also see that some particles are able to penetrate deeper into the chamber (the muons), which are able to penetrate far deeper into matter than electrons due to their greater mass (about 200 times). This greater mass *protects* them from energy losses due to electromagnetic fields and bremsstrahlung radiation when compared to electrons. In this case the primary was a proton of 10 GeV which likely interacted with a lead nucleus. The interaction of this proton with the nucleus, A, can be written as:

$$p + A \rightarrow p + X + \pi^{\pm,0} + K^{\pm,0}... \tag{1.1.1}$$
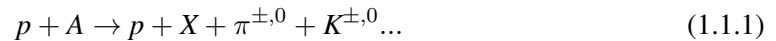
where X represents the fragmented nucleus. The proton exiting this interaction carries with it approximately 50% of the initial energy. This is know as the inelasticity, which is a global parameter that is defined as the fraction of energy given up by the leading nucleon in a collision induced by a proton or neutron impacting with a target nucleus [10].

Figuring out the nature, mass, and energy of a cosmic ray primary by looking at the image of the cloud chamber and realizing that nearly all cosmic ray studies do not benefit from watching the shower's progression can clearly be appreciated. More likely, a researcher will have but a single snapshot of the shower at a particular atmospheric depth. From this snapshot researchers must begin to determine the shower direction, the energy of the impacting primary, and its mass [11]. Colloquially, the shower direction can be extrapolated from the arrival times at the detector locations, the primary energy can roughly be determined from the number of secondary particles striking the detectors, and the overall structure of the shower depends somewhat on the mass of the primary.

More formally, in order to begin finding the energy and incoming direction of the primary, we need to find the lateral distribution function (LDF). This function, deduced from the data, is the decreasing of signals in the ground detectors as a function of distance. It is very important in the reconstruction of the shower core and direction. This density, at fixed distances from the shower core, becomes independent of the primary's mass and can be used to estimate its energy. Once the air shower reaches its maximum size, this is proportional to the energy of the primary.
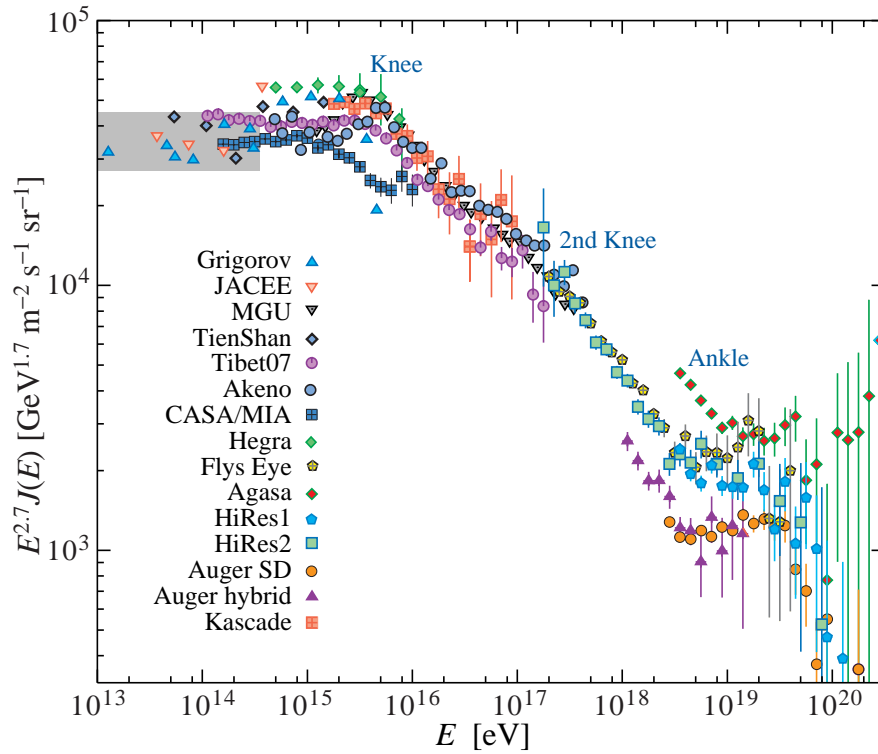
Figure 3 : All-particle spectrum of cosmic rays [12].

1.2 The Cosmic Ray (CR) Energy Spectrum

The CR spectrum spans over roughly 11 orders of magnitude of energy. Over the past several decades high altitude balloons and cleverly designed ground experiments have observed a flux that goes from 10^4 m^{-2} s^{-1} at 1 GeV to 10^{-2} km^{-2} yr^{-1} at 10^{11} GeV. If we graph the shape of this remarkable change in energy it remains quite featureless with little deviation from the constant power law,

$$J \sim E^{-\gamma}, \tag{1.2.1}$$

with $\gamma \sim 3$. The power index, γ, tends to change slightly with different energy ranges. This can be visualized by taking the product of the flux with the power of the energy. When this visualization is performed the spectrum develops into a sort of cosmic leg-like structure, as can be seen in Fig. 3. The shaping of this leg, including its slope and mass distribution, is determined by differing aspects of cosmic ray propagation, production and the distribution of sources.

The "cosmic ray knee" is a steepening in spectrum when γ goes from ~ 2.7 to 3.1 at around an energy of $\sim 10^{6.5}$ GeV. The composition of these cosmic rays relates this portion of the spectrum to the decrease of Galactic nuclear components with maximal energy E/Z [13–15] which is to be expected from an acceleration mechanism produced by confined magnetic fields where the particle's Larmor radius is smaller than the size of the accelerator itself. With this requirement along with the heaviest component being iron, the contribution to the cosmic ray spectrum from the Galaxy would be limited to about 10^8. Whether this holds is still a matter of debate as the energy end point of Galactic cosmic rays is still up for grabs.

Moving further up the energy scale to about $10^{8.7}$ GeV there appears what is called the

"second knee" where γ increases from 3.1 to 3.2. This second knee signifies the beginning of the extragalactic contribution to the cosmic ray spectrum. The nature of the vast distances traveled by these extragalactic cosmic rays exposes them to a high probability of interaction with the materials that form the interstellar medium. Below this second knee there is a further flattening of the spectrum at $\sim 10^{9.5}$ GeV. This transition, called the ankle, occurs as the power index decreases from about 3.2 to 2.7. One school of thought is that this transition coincides with the fact that the Larmor radius of a proton (within the Galactic magnetic field) exceeds the size of the actual Galaxy and that this portion of the spectrum is necessarily dominated by extragalactic cosmic rays [16].

There is popular interest in this energy range coming largely from an expectation that above about 6×10^{19} eV there should be a sharp change in the energy spectrum due to the primary's interaction with the photons that make up the Cosmic Microwave Background (CMB) [17, 18].

Once the CMB was discovered [19], it was Greisen [17], Zatsepin, and Kuzmin [18] (GZK) who pointed out that the relic photons make the universe opaque to cosmic rays of sufficiently high energy. When protons reach energies beyond the photopion production threshold the *GZK effect* (or suppression) takes effect,

$$E_{p\gamma_{\mathrm{CMB}}}^{\mathrm{th}} = \frac{m_\pi \left(m_p + m_\pi/2\right)}{\omega_{\mathrm{CMB}}} \approx 6.8 \times 10^{10} \left(\frac{\omega_{\mathrm{CMB}}}{10^{-3}\ \mathrm{eV}}\right)^{-1}\ \mathrm{GeV}, \qquad (1.2.2)$$

where m_p (m_π) denotes the proton (pion) mass and $\omega_{\mathrm{CMB}} \sim 10^{-3}$ eV is a typical CMB photon energy. After the interaction, the proton emerges with at least 50% of the incoming energy. This implies that the nucleon energy will change by a factor of e (e-folding) after propagating a distance $\lesssim (\sigma_{p\gamma}\, n_\gamma\, y_\pi)^{-1} \sim 15$ Mpc. Where $n_\gamma \approx 410$ cm^{-3} is the number density of the CMB photons, $\sigma_{p\gamma} > 0.1$ mb is the photopion production cross section, and y_π is the average energy fraction (in the laboratory system) lost by a nucleon per interaction [20]. The giant dipole resonance can be excited in a similar fashion in heavy nuclei which doesn't allow them to survive comparable distances. Extremely high energy ($\approx 10^{11}$ GeV) γ-rays that are traveling through a magnetic field ($\gg 10^{-11}$ G) a distance d, see their survival probability, $p(>d) \approx \exp[-d/6.6\ \mathrm{Mpc}]$, drop to less than 10^{-4} after 50 Mpc.

Consequently, the extreme energy ($E \geq E_{\mathrm{GZK}}$) cosmic ray (EECR) flux is consequently exceptionally low, of the order of 1 *particle/km²/sr/century*. At the high end of the spectrum, $E > 10^{11}$ GeV, it reduces to about 1 *particle/km²/sr/millennium!* Currently the leading observatories of UHECRs are ground-based observatories that cover vast areas with particle detectors overlooked by fluorescence telescopes. The largest is the Pierre Auger Observatory in Argentina, with a surface detector array comprised of 1600 water-Cherenkov detectors, covering 3000 km² which accumulates annually about 6×10^3 km² sr yr of exposure [21]. An overview of the Auger experiment is provided in Chapter 2. The more recently constructed Telescope Array (TA) covers 700 km² with 507 scintillator detectors [22], and is anticipated to annually accumulate about 1.4×10^3 km² sr yr of exposure.

1.3   Ultra-High Cosmic Ray Primaries and Motives for Their Study

It is widely accepted that the majority of UHECRs are the result of some type of magneto-hydrodynamic phenomenon in the cosmos that is able to transfer kinetic or magnetic energy into the cosmic ray. This basic approach is known colloquially as statistical acceleration. In this process the particles gain energy gradually by numerous encounters with moving magnetized plasmas. These kinds of models were mostly pioneered by Enrico Fermi [23]. For this mechanism the E^{-2} spectrum emerges very convincingly. This acceleration mechanism, however, is slow and it is difficult to keep the particles confined to the Fermi engine.

In general, the maximum attainable energy of Fermi's mechanism is determined by the time scale over which particles are able to interact with the plasma. For the efficiency of a "cosmic cyclotron" particles have to be confined in the accelerator by its magnetic field B over a sufficiently long-time scale compared to the characteristic cycle time. The Larmor radius of a particle with charge Ze increases with its energy E according to

$$
\begin{aligned}
r_L &= \sqrt{\frac{1}{4\pi\alpha}}\frac{E}{ZB} \\
&= \frac{1.1}{Z}\left(\frac{E}{\text{EeV}}\right)\left(\frac{B}{\mu\text{G}}\right)^{-1}\text{kpc}\,.
\end{aligned}
\tag{1.3.1}
$$

The particle's energy is limited as its Larmor radius approaches the characteristic radial size R_{source} of the source

$$
E_{\max} \simeq Z\left(\frac{B}{\mu\text{G}}\right)\left(\frac{R_{\text{source}}}{\text{kpc}}\right)\times 10^9\,\text{GeV}\,.
\tag{1.3.2}
$$

This limitation in energy is conveniently visualized by the 'Hillas plot' [24] shown in Fig. 4, where the characteristic magnetic field B of candidate cosmic accelerators is plotted against their characteristic size R. It is important to stress that in some cases the acceleration region itself only exists for a limited period of time; for example, supernovae shock waves dissipate after about 10^4 yr. In such a case, Eq. (1.3.2) would have to be modified accordingly. Otherwise, if the plasma disturbances persist for much longer periods, the maximum energy may be limited by an increased likelihood of escape from the region. A look at Fig. 4 reveals that the number of sources for the extremely high energy CRs around 10^{12} GeV is very sparse. For protons, only radio galaxy lobes and clusters of galaxies seem to be plausible candidates. For nuclei, terminal shocks of galactic superwinds originating in the metal-rich starburst galaxies are potential sources [26]. Exceptions may occur for sources which move relativistically in the host-galaxy frame, in particular jets from AGNs and gamma-ray bursts (GRBs). In this case, the maximal energy might be increased due to a Doppler boost by a factor ~ 30 or ~ 1000, respectively. For an extensive discussion on the potential CR-emitting-sources shown in Fig. 4, see e.g. [27].

The mechanism of acceleration of UHECRs is intimately tied to the source from which they come from. If the source of cosmic rays is properly understood, then determining the correct physical processes that led to the particle having such high energies can begin to be understood in greater detail. In order to identify UHECR sources, anisotropies must first be observed in sky maps developed from data collected at observatories. Detected anisotropies
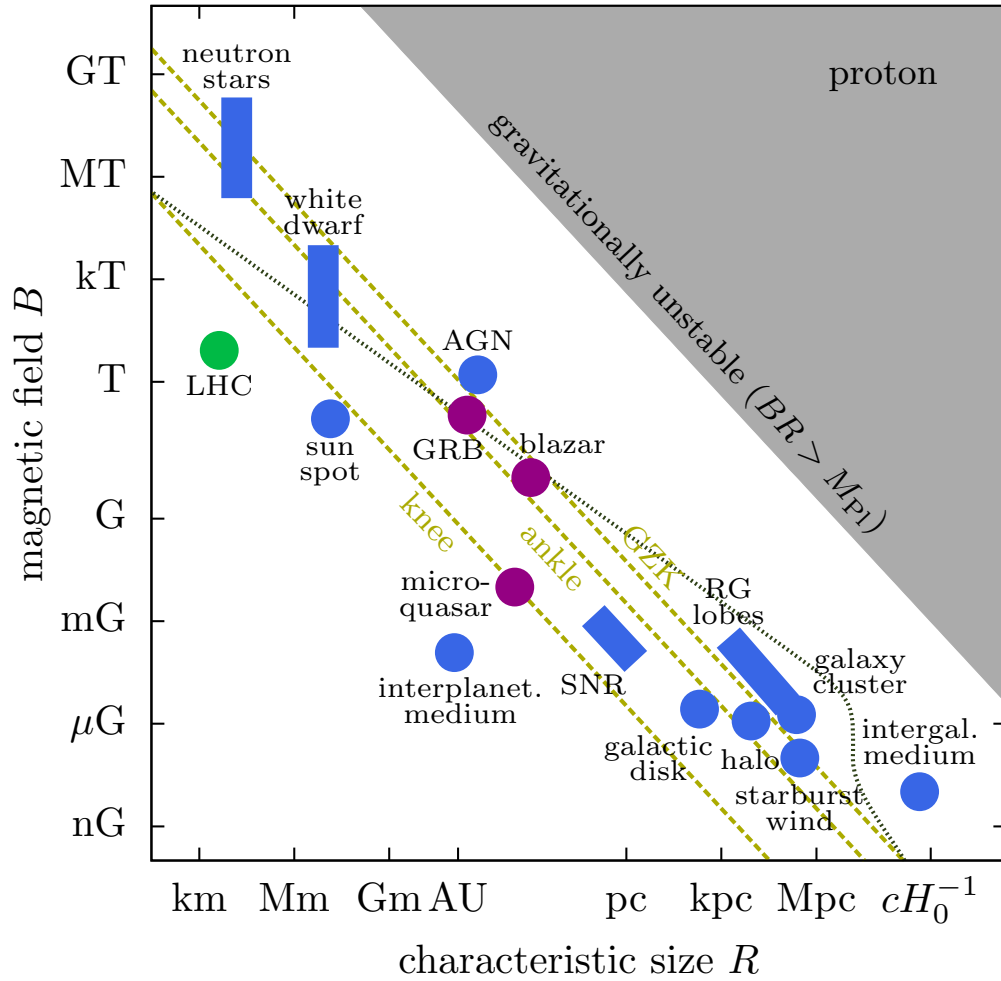
Figure 4 : The "Hillas plot" for various CR source candidates (blue areas). Also shown are jet-frame parameters for blazers, gamma-ray bursts, and microquasars (purple areas). The corresponding point for the LHC beam is also shown. The dashed lines show the *lower limit* for accelerators of protons at the CR knee ($\sim 10^{6.5}$ GeV), CR ankle ($\sim 10^{9.5}$ GeV) and the GZK suppression ($\sim 10^{10.6}$ GeV). The dotted gray line is the *upper limit* from synchrotron losses and proton interactions in the cosmic photon background ($R \gg 1$ Mpc). The grey area corresponds to astrophysical environments with extremely large magnetic field energy that would be gravitationally unstable. From Ref. [25].

would provide a wealth of data about potential sources. If the anisotropies resemble large-scale features following some type of spherical harmonic prescription then this would likely favor UHECRs coming from extragalactic sources and acceleration mechanisms based more on a statistical approach. If, however, the observed anisotropies are relatively small and center around a point in the sky they would likely represent point-like sources or astrophysical objects. This would again provide a wealth of information about possible acceleration mechanisms at the source itself and give many details about the source itself that may be unavailable using traditional astronomical message carriers, such as visible photons.

Searching for the different styles of anisotropy requires slightly different approaches based on the messenger particle, is likely to give the required directional information. While protons give us an idea of the possible acceleration mechanisms they are strongly affected by magnetic fields leaving us without point-like source information. They will, however, be able to give information on possible large-scale anisotropies. This will be discussed in Chapter 3. Neutrons,

not affected by the magnetic fields inherent to the galaxy, give us a point-like source but only have a limited effective distance before they undergo beta decay. Neutrons of high enough energy, however, should provide a survey most of the Galaxy, which will be discussed in Chapter 4. Photons are again immune to large scale magnetic fields. However, they do not give us direct information about the acceleration mechanism and are easily obstructed by dust and other cosmic debris. Although not discussed in this Thesis, there is considerable interest in searching for ultra-high energy gamma ray anisotropies [28–30]. Neutrinos, created by protons interacting with a photon field or other protons, when detected at high energies ($>$ 100 TeV) permit an exploration of the region of acceleration. Ultra-high energy cosmic neutrinos (UHEνs) emerge from the acceleration region and propagate throughout the cosmos remaining essentially unaffected by magnetic fields or dust clouds. This makes them terrific candidates for understanding point-like sources at any distance but what makes them such great candidates (their low interactivity) also makes them very difficult to detect. Despite the lower detection statistics they still have great potential. We present current limits on cosmic neutrinos in Chapter 5. Our conclusions are collected in Chapter 6.

Chapter 2

The Pierre Auger Observatory

The Pierre Auger Observatory was built with the intention to measure the flux, arrival direction, and the mass composition of the highest energy CRs, those with energies $E \geq 10^{18}$ eV, whose origin and exact acceleration mechanism have been a mystery to researchers for many years.

The original design for the Pierre Auger Observatory was formulated through workshops that started in Paris in 1992 [31] and finished in a 6-month study at the Fermi National Accelerator Laboratory in 1995 [32]. This design outlined a northern and southern observatory. The Southern observatory called for 1600 water-Cherenkov detectors, arranged on a triangular grid, with sides being 1.5 km, overlooked from 4 sites by optical stations, each containing 6 air-fluorescence light telescopes. While the water tanks pick up the particle component (made up mainly of muons, electrons, and positrons) the fluorescence cameras measure the emission from nitrogen molecules within the atmosphere that come from their interactions with charged shower particles. These two techniques have an established history studying extensive air showers (EAS) and are brought together at the Pierre Auger Observatory to collect data in tandem, so called *hybrid events*, allowing for the two detector systems to calibrate each other, provide a greater sensitivity to composition, and collect additional data that would not be available individually. Shown in Fig. 5, the layout of the hybrid system contains 1600 surface stations, 24 air fluorescence telescopes, and covers roughly 3000 km^2.

The location chosen to host the Southern site was Pampa Amarilla ($35.1° - 35.5°S, 69.0° - 69.6°W$ and 1300-1400 m above sea level) which lies in the south of the Province of Mendoza, Argentina and is close to the city of Malargüe. The altitude, relatively flat topography, and optical characteristics similar to those required for astronomical telescopes, made the site highly desirable. It also has an excellent view of the Galactic center, a possible source of UHECRs [33]. Construction of the Southern site was completed in 2008. The deployment of the Northern site has now been canceled.

2.1 The Fluorescence Detector

When a primary cosmic ray strikes the atmosphere, it generates an EAS. The charged particles that make up this EAS excite atmospheric nitrogen molecules which then emit fluorescent light
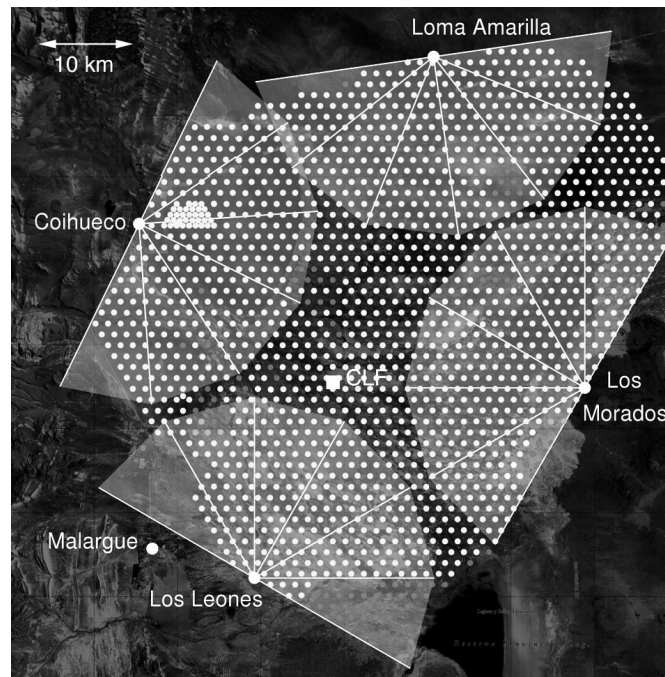
Figure 5 : Status of the Pierre Auger Observatory as of March 2009. Gray dots show the positions of surface detector stations, lighter gray shades indicate deployed detectors, while dark gray defines empty positions. Light gray segments indicate the fields of view of 24 fluorescence telescopes which are located in four buildings on the perimeter of the surface array. Also shown is a partially completed infill array near the Coihueco station and the position of the Central Laser Facility (CLF, indicated by a white square) [34]

in the range of 300-430 nm. The number of photons that are emitted during this process is proportional to the energy that was deposited in the atmosphere due to the electromagnetic energy losses by the charged particles. Measuring the rate of the fluorescence emission as a function of of atmospheric slant depth, X, the air fluorescence detector measures the *longitudinal development profile*, $\frac{dE}{dX}$ of the air shower. The integral of this development profile gives the amount of energy that was lost electromagnetically. This electromagnetic energy loss accounts for about 90% of the total energy of the primary.

Using nitrogen fluorescence emission induced by extensive air showers to study UHECRs is a well-established method that was used prior to the Pierre Auger Observatory in the Fly's Eye [35] and HiRes [36] experiments. The fluorescence detector (FD) of the Pierre Auger Observatory consists of four observation sites that can be seen in Fig. 5. The sites (Los Leones, Los Morados, Loma Amarilla, and Coihueco) are located on top of small elevations overlooking the SD array. Within each FD site there are housed 6 independent telescopes with a field of view of $30° \times 28.6°$ in azimuth and elevation giving a $180°$ coverage in azimuth when combined [34] (see Fig. 6).

Figure 7 shows the basic cross section of an individual FD telescope. The basic components of the optical system are the optical filter at the entrance window, a circular aperture, a corrector ring, a segmented mirror, and a 440 PMT camera. The optical filter absorbs visible light while transmitting UV photons up to 410 nm in wavelength. This allows nearly the entire nitrogen fluorescence spectrum through while not allowing the signals to be lost in a haze of visible
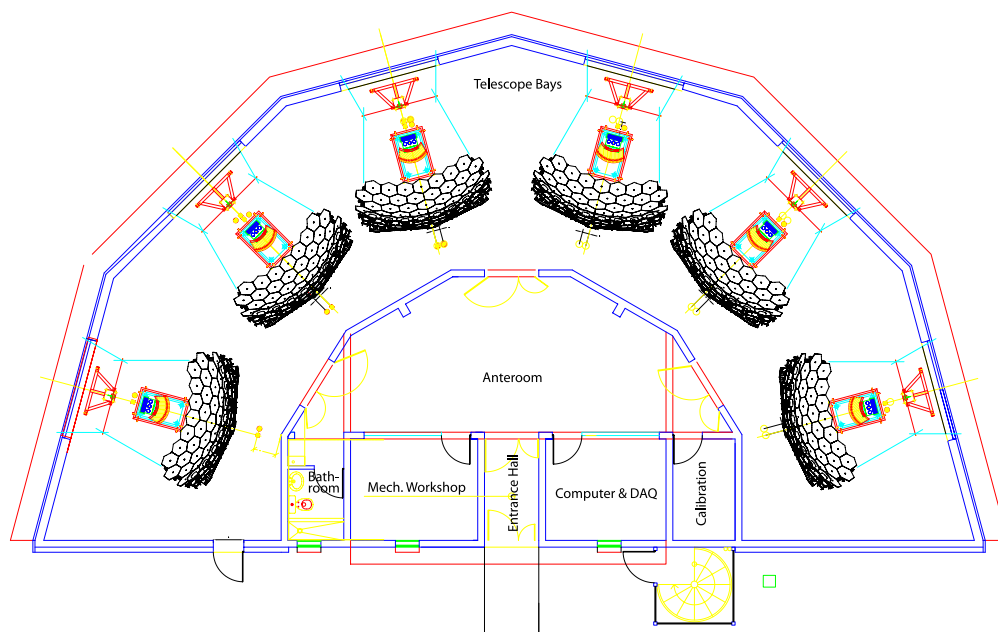
Figure 6 : Schematic layout of the building with six fluorescence telescopes [34].
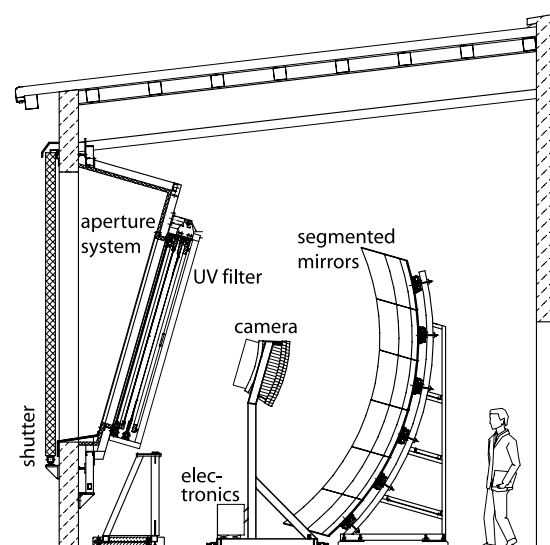

Figure 7 : Schematic view of a fluorescence telescope of the Pierre Auger Observatory [34].

photon noise. Inside the filter is the corrector ring which makes up part of a Schmidt camera design that eliminates coma aberration and helps to correct the spherical aberration [34, 37].

Recording widely varying signals with a background of continuously changing light, the FD telescopes present a challenge for the electronics design and the data acquisition system (DAQ). The DAQ must provide a large dynamic range and strong background rejection, while still accepting anything that is plausibly an air shower. A plausible shower or FD event is determined by a sequence of triggered PMTs. It must also allow for remote operation of the FD telescopes and the absolute FD-SD timing offset must be accurate to enable reliable hybrid event reconstruction.

2.2 The Surface Detector Array

The surface detector array (SD) consists of 1600 water-Cherenkov detectors that are arranged on a triangular grid framework with 1.5 km spacings. This framework covers an area of approximately 3000 km^2 and detects the secondary particles produced when a primary cosmic ray interacts with the atmosphere. The particle densities are measured as the shower strikes the ground just past the EAS's maximum development [38]. This information can then be used to develop the lateral density distribution (LDF).

Because of their durability and relatively low cost, water- Cherenkov detector were chosen for the surface array. In addition, they also exhibit a uniform exposure up to large zenith angles and are not only sensitive to charged particles, but also to energetic photons [21].

Each surface station is constructed using a 3.6 m diameter and 1.6 m high cylindrical water tank containing a sealed liner with a reflective inner surface that conforms to the hard outer shell (see Fig. 8). The liners are made of a plastic material produced from a laminate composed of an opaque three-layer polyethylene bonded to a layer of Tyvek$^{\circledR}$ by a layer of TiO$_2$ pigmented polyethylene. The polyethylene layer was chosen for strength and flexibility while the Tyvek$^{\circledR}$ for its reflectivity and its ability to minimize chemical leaching into the water. This liner is filled with 12000 liters of ultra-pure water in order to achieve the lowest possible UV Cherenkov light attenuation and to produce consistent results during the 20 year detector lifetime [21].

The Cherenkov light produced by air shower particles passing through the water is picked up by three 9-inch diameter photomultiplier tubes (PMTs) that are shielded from outside light and distributed symmetrically 1.2 m from the center of the tank and look into the water through UV transparent windows. A solar power system provides the PMTs with power along with an electronics package that contains a microprocessor, GPS receiver, radio transceiver, and a power controller. This solar power system gives the surface stations the ability to be self sufficient [38].

When Cherenkov light is detected, each PMT produces two signals which are digitized by 40 MHz 10-bit Flash Analogue to Digital Converters (FADCs). The two signals taken from different areas of the PMT (the anode and last dynode) provide an ample dynamic range to precisely cover the signals produced in the detectors near the shower core and those produced far from the core. Once a candidate shower event triggers the surface detector array, the signals from 3 PMTs are sent to the central data acquisition system (CDAS) where the event can then
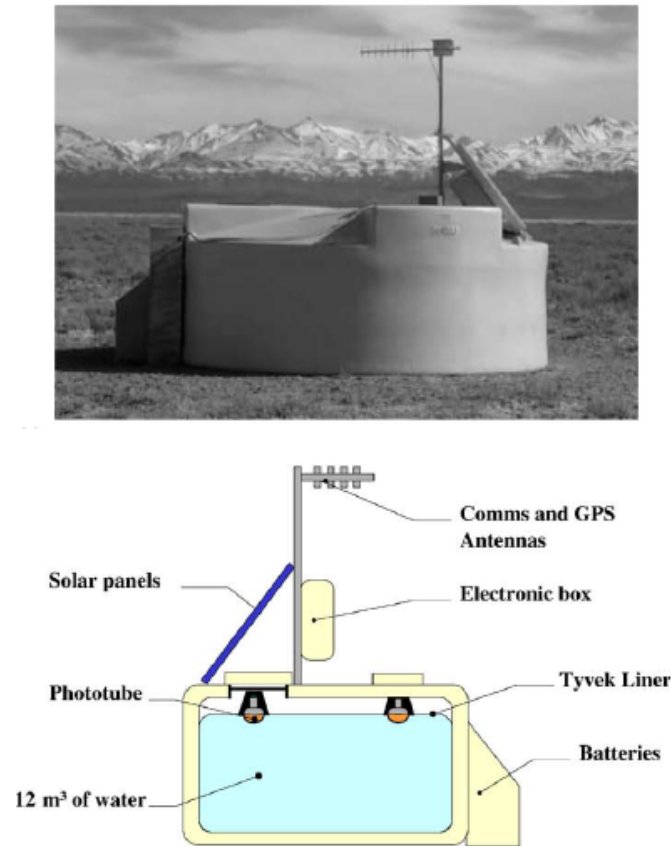
Figure 8 : Top: A photograph if an surface detector water tank. Bottom: Schematic of the surface detector tank [37].

be reconstructed [21].

2.3   Energy and Angular Resolution

Using a shower front model, the arrival direction of a SD event can be found by fitting the arrival time of the first particle in each station. How accurate the arrival direction is depends on how precise the clock on the detector is, as well as arrival time fluctuations. This timing uncertainty is modeled directly from data in each station and is adjusted based on information provided by pairs of adjacent stations [39]. The angular resolution, which is dependent on the primary energy, is defined as the radius of circular solid angle that would include 68% of the reconstructed events that arrive from a fixed direction [40].

SD event signals are quantified by comparing the signal response to the equivalent response of a SD to a muon traveling vertically and centrally through it, the so-called *vertical equivalent muon* or VEM. The energy for the air shower is then found by fitting the SD signal that a station would have measured for a VEM located 1000 meters from the core of the shower, $S(1000)$. An energy estimator is then used, $S_{38°}$, which is independent of the zenith angle of the actual event. $S_{38°}$ is the energy that an event would have produced had $S(1000)$ arrived at the median zenith angle of $38°$. The energy estimator is calibrated using a subset of high quality hybrid events where the geometry is determined from the FD and supplemented by the time at the SD

with the highest signal. This calibration comes with a 22% systematic uncertainty and a 15% uncertainty in SD energy determination. For a greater detailed discussion, see [41, 42].

By choosing the target size according to the angular resolution of the SD, the sensitivity to potential point-like sources can be optimized. The angular resolution, ψ, corresponds to the 68% containment radius for each energy looked at. The point spread function was taken to be,

$$p(\theta) = \frac{\theta}{\sigma^2} exp(-\theta^2/2\sigma^2) \,, \qquad (2.3.1)$$

where, θ represents the angle between the reconstructed direction and the true arrival direction and σ can be identified as $\psi/1.51$ by the 68% containment definition for the angular resolution, ψ. By selecting only events within a hard cut on the angle from the target center, top-hat counting, the signal-to-noise ratio is optimized by the top-hat radius χ, which is given by $\chi = 1.59\sigma = 1.05\psi$.

The SD's angular resolution is dependent on energy and improves slightly at large zenith angles. Some declinations can only be viewed at large zenith angles because of which there is also some dependence on the declination within the angular resolution, ψ, as well.

2.4 Discovery of the GZK Suppression?

The most recently uncovered feature of the cosmic ray spectrum is a sharp and statically very significant suppression of the flux. In 2007, the HiRes Collaboration reported a suppression of the CR flux above $E = [5.6 \pm 0.5(\text{stat}) \pm 0.9(\text{syst})] \times 10^{19}$ eV, with 5.3σ significance [43]. The spectral index of the flux steepens from 2.81 ± 0.03 to 5.1 ± 0.7. The discovery of the suppression has been confirmed by the Pierre Auger Collaboration, measuring $\gamma = 2.69 \pm 0.2(\text{stat}) \pm 0.06(\text{syst})$ and $\gamma = 4.2 \pm 0.4(\text{stat}) \pm 0.06(\text{syst})$ below and above $E = 4.0 \times 10^{19}$ eV, respectively (the systematic uncertainty in the energy determination is estimated as 22%) [41].

In 2010, an updated Auger measurement of the energy spectrum was published [44], corresponding to a surface array exposure of $12,790$ km^2 sr yr. This measurement, combining both hybrid and SD-only events, is shown in Fig. 9. The so-called "ankle" feature and the flux suppression are clearly visible. A broken power law fit to the spectrum shows that the break corresponding to the ankle is located at $\log_{10}(E/\text{eV}) = 18.61 \pm 0.01$ with $\gamma = 3.26 \pm 0.04$ before the break and $\gamma = 2.59 \pm 0.02$ after it. The break corresponding to the suppression is located at $\log_{10}(E/\text{eV}) = 19.46 \pm 0.03$. Compared to a power law extrapolation, the significance of the suppression is greater than 20σ.

The existence of this suppression is consistent with the GZK predictions [17, 18], in which CR interactions with the CMB photons rapidly degrade the CR energy, limiting the distance from which UHECR can travel to ~ 100 Mpc. If the primary CRs are protons, the dramatic energy degradation proceeds via resonant photopion production in the CMB. If the primary cosmic rays are heavy nuclei, successive photoevaporation of one or two nucleons through the giant dipole resonance is mainly responsible for the UHECR energy loss.

Though this suppression in the energy spectrum is consistent with the GZK prediction, it is not necessarily the case that it is the *result* of the GZK effect. The suppression may also
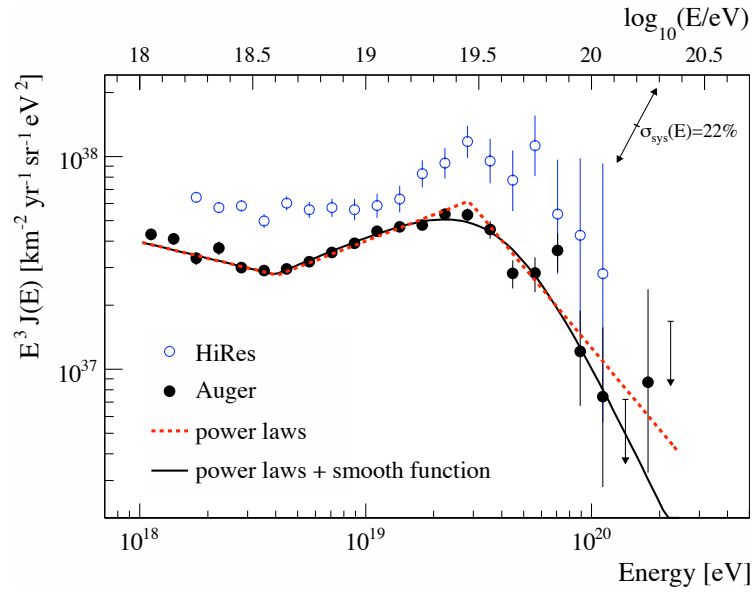
Figure 9 : Combined spectrum from Auger (hybrid and SD events) and the stereo spectrum HiRes. The Auger systematic uncertainty of the flux scaled by E^3, due to the uncertainty of the energy scale of 22%, is indicated by arrows. The results of the two experiments are consistent within systematic uncertainties. From Ref. [44].

simply represent the maximum energy attainable in nearby extragalactic cosmic accelerators, $E^{\max}$, which, perversely enough, might happen to fall in the area where the GZK feature would be expected. One model has been proposed [45] in which proton acceleration ceases beyond an energy $E_{\mathrm{p}}^{\max} \sim 4 \div 6$ EeV, while the maximum energy attainable by nuclei is a factor of Z larger, or about $1 \div 2 \times 10^{20}$ eV for the case iron. In this scenario, the ankle signifies the maximum accessible proton energy. Above these energies, the composition would then be dominated by heavy nuclei. The model is consistent with Auger measurements of the depth at which air showers reach their maximum size, $X_{\max}$ and the $X_{\max}$ fluctuations, $\mathrm{RMS}(X_{\max})$, which do indicate a trend to heavier composition with increasing energy [46].

Ultimately sorting out the situation in the GZK region of the spectrum will not be a simple undertaking. For one thing, there is some tension between the results from different experiments. While the Auger results indicate an increase in average primary mass with energy, the results of the HiRes experiment are consistent with proton dominance of the spectrum up to the highest energies [47]. Results from the Telescope Array are also consistent with pure proton composition [22], though statistics are limited at present[1].

With sufficient statistics, additional telltale spectral features will emerge if the suppression is indeed a consequence of the GZK effect. For instance, if $E^{\mathrm{max}} > E^{\mathrm{GZK}}$, then the energy spectrum should recover, or flatten out, beyond the GZK cutoff region. The details of this recovery will depend on the UHECR composition. Furthermore increased statistics should also uncover a hitherto unobserved feature. *Ensemble fluctuations* should eventually appear in the energy spectrum [48]. Ensemble fluctuations constitute variations in the energy distribution in excess of those expected from Poisson statistics. These fluctuations are a consequence of

---

[1]It should be noted that the analysis techniques employed by the Auger collaboration are different from those used by the HiRes and TA collaborations.

the catastrophic energy losses suffered when protons or nuclei interact in the CMB as well as the discrete redistribution of energy among nuclear fragments if the UHECR flux contains heavy nuclei. The magnitude and fine structure of ensemble fluctuations depend on the density of UHECR sources, the composition of the UHECR, and propagation effects, and hence will provide complementary information on the sources, composition and propagation of CR's.

Identifying the arrival directions of the highest energy events is also important not only for revealing the CR accelerators but also for correctly interpreting the meaning of the suppression. For instance, an initially tantalizing observation by the Pierre Auger Observatory of a correlation between UHERC arrival directions and nearby Active Galactic Nuclei [49, 50] hinted that the primary UHECR were likely protons, owing to the small $\sim 3°$ separation angle characterizing the correlation between CR arrival directions and candidate sources. Furthermore, since the correlation was strongest for events within about 75 Mpc, the observation appeared to indicate that the spectral suppression is indeed the GZK effect. Additional Auger data [51] have not, however, increased the significance of the correlation, however, so at present the situation is much less clear.

Altogether there exists a complex of features at the end of the UHECR spectrum which must be understood in order to pin down UHECR origins and composition. Characterizing these features is an exceedingly difficult task owing to the rarity of the highest energy events. In this Thesis we take a grand first step in the right direction by searching for anisotropies in the distribution of arrival directions.

Chapter 3

Search for Large Scale Anisotropies

3.1 General Idea

When searching for clues as to the origin of UHECRs, the detection of anisotropies in the sky as a function of energy will be able to give the best clues on where to look. If cosmic ray events cluster in a small angular region associated with compact astrophysical objects, it is feasible that these could then be associated with UHECR sources. If, however, the distribution of events has a large scale anisotropy then it is more likely that UHECRs are associated with large-scale structures in the universe, such as the Galactic Plane, nearby galaxy groups, or the local Supercluster of galaxies.

A popular belief is that the "ankle" in the cosmic ray energy spectrum located around 4×10^{18} eV [52–54] is the result of the cosmic ray origin shifting from Galactic to extragalactic sources [55, 56]. Determining the energy that the intensity of extragalactic cosmic rays start to predominate the galactic intensity is an important step to understanding the origin as well as the evolution of acceleration mechanisms of UHECRs. The amplitude and shape of large scale anisotropies, which would signal the transition, are uncertain at this point since they are dependent on the model chosen to describe the galactic magnetic field, the charges of cosmic rays, and the assumed source distribution.

For heavy cosmic ray primaries originating from stationary sources within the Galaxy, there are some estimates based on models of diffusion and drift motions [57] as well as those based on the direct integration of trajectories [58] that show dipolar anisotropies of a few percent could be revealed in the energy range just below the ankle. If the primaries are light however, then amplitude could be even larger unless the sources are strongly intermittent and pure diffusion motions hold up to EeV energies [59, 60].

If, above 1 EeV, primaries are predominantly of extragalactic origin [61–63] then their angular distribution should be very isotropic. It is possible, however, that due to the translational motion of the Galaxy relative to a stationary extragalactic UHECR rest frame, a dipole could be produced in a way similar to the *Compton-Gettering effect*. In addition to the general translation motion it is likely that the rotation of the Galaxy would be able to produce an anisotropy due to the moving magnetic fields. UHECRs traversing through far away regions of the Galaxy will experience an electric force from the relative motion of the system in which the field is purely

magnetic [64]. These moving magnetic fields are expected to transform even a relatively simple Compton-Gettering dipole into something much more complex being described by higher order multipoles [64].

Clearly large scale UHECR arrival distributions as a function of their energy is very important to the understanding of their origin. Recently reported by the Pierre Auger Observatory [65], using the large amount of data collected via the SD array, were the results of a first harmonic analysis of the right ascension distribution performed for different energy ranges above 0.25 EeV. From this study the most stringent bounds were able to be put on the upper limits of the dipole component in the equatorial plane, below 2% at a 99% confidence level for EeV energies. The SD array benefits from an almost uniform directional exposure in right ascension due to Earth's rotation which is very effective at picking up any dipolar modulation in that coordinate. Using this technique alone however limits the sensitivity to dipolar modulation along the Earth's rotational axis. In order to obtain a more complete picture of possible large scale anisotropies the search must include not only the dipole component of the right ascension but also in declination which can be obtained from the large amount of data collected by the Pierre Auger Observatory to analyze the dipolar and quadrupolar harmonics.

3.2 The Large Scale Anisotropy Data Set

The data used to find the upper limits for possible dipolar and quadrupolar anisotropies in the harmonic analysis of the right ascension and declination was made up of events recorded by the SD array from January 1, 2004 through December 31, 2011, with zenith angles less than $55°$. In order to get good directional and energy reconstructions, events must meet certain criteria. For each event, the *elemental cell* (which is the name given to the six neighbors of the water-Cherenkov detector with the highest signal) is fully active when the event was recorded [21]. Based on selection criteria and by accounting for periods of instability within the array, the total geometric exposure of the data set is 23,520 km^2 yr sr.

The event arrival direction is determined using a shower front model developed in [39]. More details will also be given in section 4.2.1. The angular resolution is $\sim 2.2°$ for the lowest energies that were observed and becomes $\sim 1°$ at the highest energies observed [39]. This resolution is adequate to perform the large scale anisotropy surveys.

3.3 Control of the Event Counting Rate

For searches of large scale anisotropies, controlling the event counting rate is critical. The energy spectrum is relatively steep which means that any mild bias in the estimate of the shower energy with time or zenith angle can lead to a significant distortion of the event counting rate. As stated in the previous section, for the SD array the energy estimator is given by the signal at 1000 m from the shower core or $S(1000)$. At any energy, extensive air showers are dependent on the atmospheric pressure and the air density which means of course that so is $S(1000)$. Over time, variations in $S(1000)$ lead to variations of the event rate that can distort the dependence of the cosmic ray intensity with right ascension. In order to correct with these variations, the observed

shower size $S(1000)$ measured at the actual air density and pressure is related to $S_{atm}(1000)$ which is what would have been measured at reference values of density and pressure [66]. By using the reference values, which are chosen from averages at Malargüe, and applying the subsequent corrections to the energy assignments of the showers, the spurious variations of the event rate in right ascension can be canceled.

In addition to atmospheric effects, geomagnetism also plays a role. The charged particles that make up parts of extensive air showers are influenced by Earth's magnetic field, curving their trajectories and thus broadening their spatial distribution in the direction of the Lorentz force. The component of the geomagnetic field strength perpendicular to arrival direction is dependent on both the zenith and azimuthal angles. This field induces small changes in the density of particles at the ground which break the circular symmetry of the lateral spread of the particles, thereby inducing a dependence of the shower size $S(1000)$ as a fixed energy in terms of the azimuthal angle. From the energy spectrum's steepness the azimuthal dependence translates into azimuthal modulations of the estimated cosmic ray event rate at any given $S(1000)$. In order to take this effect into account, the observed shower size is related to the one that would have been observed in the geomagnetic fields absence, $S_geom(1000)$ [21].

Once atmospheric and geomagnetic effects are taken into account for $S(1000)$, its dependence on zenith angle due to attenuation of the shower and geometrical effects can be taken into account using the constant intensity method [41] which was briefly described in the previous section. Simply speaking, the shower signal is converted to the value that would have been expected had the shower arrived at a zenith angle of $38°$. The reference shower signal is then converted into energy using a calibration curve based on hybrid events [41].

3.4 Direction Exposure above 1 EeV

Accurately determining the effective time-integrated collecting area for a flux from each direction of the sky, known as the *directional exposure*, ω, of the Pierre Auger Observatory and given in units of km^2 yr sr, is critical when searching for anisotropies. When energies are below 3 EeV the directional exposure is controlled by the detection efficiency, ϵ, for triggering, which is dependent on the energy, E, the zenith angle, θ, and the azimuth angle, ϕ. The directional exposure at Pierre Auger is maximized above 3 EeV and becomes smaller at lower energies where the detection efficiency is less.

The criteria to select high quality events allows for the precise determination of the geometric directional aperture per cell as $a_{\text{cell}}(\theta) = 1.95 \; \cos\theta \; \text{km}^2$ [21]. This also lets us use the array's regularity to obtain its geometric directional aperture as a simple multiple of $a_{\text{cell}}(\theta)$ [21]. The number of element cells, $n_{\text{cell}}(t)$, is continuously monitored at the Pierre Auger Observatory. Accounting for the modulation imprinted by $n_{\text{cell}}(t)$ variations in the expected number of events at the $sidereal periodicity$, T_{sid}, is necessary when searching for large scale anisotropies. Following the treatment in Ref. [44], within each sidereal day the local sidereal time, α^0, is expressed either in hours or radians depending when it is appropriate and is chosen so that it is equal to the right ascension of the zenith at the center of the array. The total number of elemental

cells, expressed as a function of α^0, and its associated variations $\Delta N_{\text{cell}}(\alpha^0)$ are given as,

$$N_{\text{cell}}(\alpha^0) = \sum_j n_{\text{cell}}(\alpha^0 + jT_{sid}), \qquad \Delta N_{\text{cell}}(\alpha^0) = \frac{N_{\text{cell}}(\alpha^0)}{\langle N_{\text{cell}}\rangle_{\alpha^0}}, \qquad (3.4.1)$$

where,

$$\langle N_{\text{cell}}\rangle_{\alpha^0} = 1/T_{sid} \int_0^{T_{sid}} \mathrm{d}\alpha^0 N_{\text{cell}}(\alpha^0), \qquad (3.4.2)$$

Continuing with the same treatment as in Ref. [44], a weighting factor that is inversely proportional to $\Delta N_{\text{cell}}(\alpha^0_k)$ can be applied to each event k to take into account the small modulation of the expected number of events in the right ascension induced by variations when estimating anisotropy parameters. This allows the growth of the SD array to be accounted for.

The directional exposure in celestial coordinates for each elemental cell is obtained through the integration over the local sidereal time of $x^{(i)}(\alpha^0) \times a_{\text{cell}}(\theta) \times \epsilon(\theta, \varphi, E)$, where $x^{(i)}(\alpha^0)$ is the operational time of the cell (i) and $\epsilon(\theta, \varphi, E)$ is the detection efficiency function. Because the small modulations in the time imprinted in the event counting rate by experimental effects is accounted for by the weighting factor, the small variations in the local sidereal time for each $x^{(i)}(\alpha^0)$ can be neglected when finding ω. The zenith and azimuthal angles can be related to the declination and the right ascension by,

$$
\begin{aligned}
\cos\theta &= \sin\delta \sin\ell_{\text{site}} + \cos\delta \cos\ell_{\text{site}} \cos(\alpha - \alpha^0), \\
\tan\varphi &= \frac{\cos\delta \sin\ell_{\text{site}} \cos(\alpha - \alpha^0) - \sin\delta \cos\ell_{\text{site}}}{\cos\delta \sin(\alpha - \alpha^0)},
\end{aligned} \qquad (3.4.3)
$$

Where ℓ_{site} is the mean latitude of the Pierre Auger Observatory. Because θ and φ depend only on the difference, $\alpha - \alpha^0$, the integration over α^0 can then be substituted for an integration over the hour angle $\alpha' = \alpha - \alpha^0$ so that the directional exposure actually does not depend on right ascension when the $x^{(i)}$ are assumed to be independent of local sidereal. Thus giving,

$$\omega(\delta, E) = \sum_{i=1}^{n_{\text{cell}}} x^{(i)} \int_0^{24h} \mathrm{d}\alpha' \, a_{\text{cell}}(\theta(\alpha', \delta)) \, \epsilon(\theta(\alpha', \delta), \varphi(\alpha', \delta), E). \qquad (3.4.4)$$

The dependence on the zenith angle by the detection efficiency $\epsilon(\theta, \varphi, E)$ can be found directly from empirical data based on the quasi-invariance of the zenithal distribution to large scale anisotropies for zenith angles less than $\simeq 60°$ and because the Pierre Auger Observatory is far from the poles of the Earth [67]. In addition tp the azimuthal dependence of the efficiency due to geomagnetic effects, the corrections to both the geometric aperture of each elemental cell and the detection efficiency due to the tilt of the array, and the corrections due to the spatial extension of the array can impact ω. These effects have all been accounted for in Ref. [67] and the resulting expression for ω is,

$$\omega(\delta, E) = \sum_{i=1}^{n_{\text{cell}}} x^{(i)} \int_0^{24h} \mathrm{d}\alpha' \, a_{\text{cell}}^{(i)}(\theta, \varphi) \, [\epsilon(\theta, \varphi, E) + \Delta\epsilon_{\text{tilt}}(\theta, \varphi, E)], \qquad (3.4.5)$$

where $a_{\text{cell}}^{(i)}$ is the geometrical directional aperture per cell which is no longer given by just $\cos(\theta)$ but is now dependent upon both θ and φ which is due to the tilt of the array. The array tilt also

induces an additional variation of the detection efficiency with azimuth below 3 EeV for which the correction is represented by $\Delta\epsilon_{\mathrm{tilt}}(\theta, \varphi, E)$. Both θ and φ depend on α', δ and $\ell_{\mathrm{cell}}^{(i)}$ [67].

The detection efficiency at high zenith angles, down to 1 Eev, is high enough that the equatorial south pole is visible at any time and hence constitutes the direction of maximum exposure. For a wide range of declinations between $\simeq -89°$ and $\simeq -20°$, the directional exposure is $\simeq 2,500$ km^2 yr at 1 EeV, and $\simeq 3,500$ km^2 yr for any energy above full efficiency. Then, at higher declinations, it smoothly falls to zero, with no exposure above $\simeq 20°$ declination [68].

3.5 Searching for Large Scale Patterns

3.5.1 Estimating Spherical Harmonic Coefficients

Following the formulation in reference [67], over a sphere, $\Phi(\mathbf{n})$, any angular distribution can be decomposed in terms of a multipolar expansion,

$$\Phi(\mathbf{n}) = \sum_{\ell \geq 0} \sum_{m=-\ell}^{\ell} a_{\ell m} Y_{\ell m}(\mathbf{n}), \tag{3.5.1}$$

where $\mathbf{n}$ represents a unit vector in equatorial coordinates. The common method is to extract each multipolar coefficient which makes use of the completeness relation of spherical harmonics,

$$a_{\ell m} = \int_{4\pi} \mathrm{d}\Omega \, \Phi(\mathbf{n}) Y_{\ell m}(\mathbf{n}). \tag{3.5.2}$$

The integration is done over the entire sphere of directions Within the spherical harmonic coefficients, $a_{\ell m}$, any anisotropic information will be encoded. Variations on an angular scale of Θ radians contribute amplitude in the $\ell \simeq 1/\Theta$ modes.

It is impossible to estimate the multipolar coefficients, $a_{\ell m}$, using this method in the case of partial sky coverage because the solid angle exposure in the sky is zero. The unseen solid angle prevents one from making use of the completeness relation of the spherical harmonics [69, 70]. Since the combination of the angular distribution, $\Phi(\mathbf{n})$, and of the directional exposure function, $\omega(\mathbf{n})$, are what make up the observed arrival direction distribution, the integration performed in Eq. 3.5.2 does not allow the extraction of the multipolar coefficients of $\Phi(\mathbf{n})$, but only those of $\omega(\mathbf{n}) \Phi(\mathbf{n})$ [71]. We then find,

$$
\begin{aligned}
b_{\ell m} &= \int_{\Delta\Omega} \mathrm{d}\Omega \, \omega(\mathbf{n})\Phi(\mathbf{n})Y_{\ell m}(\mathbf{n}) \\
&= \sum_{\ell' \geq 0} \sum_{m'=-\ell'}^{\ell'} a_{\ell' m'} \int_{\Delta\Omega} \mathrm{d}\Omega \, \omega(\mathbf{n})Y_{\ell' m'}(\mathbf{n})Y_{\ell m}(\mathbf{n}).
\end{aligned} \tag{3.5.3}
$$

The $a_{\ell m}$ coefficients are related to the $b_{\ell m}$ coefficients by $b_{\ell m} = \sum_{\ell' \geq 0} \sum_{m'=-\ell'}^{\ell'} [K]_{\ell m}^{\ell' m'} a_{\ell' m'}$. Imprinting the interferences between modes induced by the non-uniform and partial coverage of the sky, the K matrix is determined by the directional exposure.

$\overline{\mathrm{d}N}(\mathbf{n})/\mathrm{d}\Omega$ (the observed arrival direction distribution) provides an estimation of the $b_{\ell m}$ coefficients through,

$$\bar{b}_{\ell m} = \int_{\Delta\Omega} \mathrm{d}\Omega \, \frac{\overline{\mathrm{d}N}(\mathbf{n})}{\mathrm{d}\Omega} Y_{\ell m}(\mathbf{n}), \tag{3.5.4}$$

where the observed arrival direction distribution of an set of N arrival directions $\{\mathbf{n}_1, ..., \mathbf{n}_N\}$ can be modeled as a sum of Dirac functions on the sphere. If $\Phi(\mathbf{n})$ has no higher moments than $\ell_{\max}$, then the first $b_{\ell m}$ coefficients with $\ell \leq \ell_{\max}$ are related to non-vanishing $a_{\ell m}$ by the square matrix $K_{\ell_{\max}}$ which is truncated to $\ell_{\max}$. By inverting this matrix it allows the recovery of the underlying $a_{\ell m}$ coefficients from the measured $b_{\ell m}$,

$$\overline{a}_{\ell m} = \sum_{\ell'=0}^{\ell_{\max}} \sum_{m'=-\ell'}^{\ell'} [K_{\ell_{\max}}^{-1}]_{\ell m}^{\ell' m'} \overline{b}_{\ell' m'}. \tag{3.5.5}$$

The recovered resolutions for the $\overline{a}_{\ell m}$ coefficient for small anisotropies ($|a_{\ell m}|/a_{00} \ll 1$) is proportional to $\left([K_{\ell_{\max}}^{-1}]_{\ell m}^{\ell m} \right)^{0.5}$ [71], where

$$\sigma_{\ell m} = \left([K_{\ell_{\max}}^{-1}]_{\ell m}^{\ell m} \overline{a}_{00} \right)^{0.5}. \tag{3.5.6}$$

Assuming that the energy dependence of the angular distribution of cosmic rays is sufficiently smooth so that multipolar coefficients can be considered constant for energy, E, within a narrow interval, ΔE. Considering the directional exposure to be independent of the right-ascension [67]. The expected arrival direction distribution within an interval, ΔE, is

$$\frac{dN(\mathbf{n})}{d\Omega} \propto \tilde{\omega}(\delta) \sum_{\ell \geq 0} \sum_{m=-\ell}^{\ell} a_{\ell m} Y_{\ell m}(\mathbf{n}), \tag{3.5.7}$$

where the effective directional exposure for the energy interval, ΔE, is represented by $\tilde{\omega}(\delta)$, which is normalized such that,

$$\tilde{\omega}(\delta) = \frac{\int_{\Delta E} dE \; E^{-\gamma} \omega(\delta, E)}{\max_{\delta} \left[\int_{\Delta E} dE \; E^{-\gamma} \omega(\delta, E) \right]}, \tag{3.5.8}$$

with γ being the spectral index in the considered energy range. For any direction in the sky this function provides the effective directional exposure in the energy range ΔE. To correct for a slightly not-uniform directional exposure in right ascension the observed arrival direction distribution is modeled as a sum of Dirac functions on a sphere weighted by the factor $\Delta N_{\text{cell}}^{-1}(\alpha_k^0)$ for each event recorded. From this, the integration from Eq. 3.5.3 becomes,

$$\overline{b}_{\ell m} = \sum_{k=1}^{N} \frac{Y_{\ell m}(\mathbf{n}_k)}{\Delta N_{\text{cell}}(\alpha_k^0)}. \tag{3.5.9}$$

This allows the $\overline{a}_{\ell m}$ multipolar coefficients to be recovered using Eq. 3.5.5.

3.5.2 Looking for Dipolar Patterns

If the angular distribution of cosmic rays is modulated by a pure dipole (the intensity) $\Phi(\mathbf{n})$ can be parameterized in any direction $\mathbf{n}$,

$$\Phi(\mathbf{n}) = \frac{\Phi_0}{4\pi} \left(1 + r \, \mathbf{d} \cdot \mathbf{n} \right), \tag{3.5.10}$$
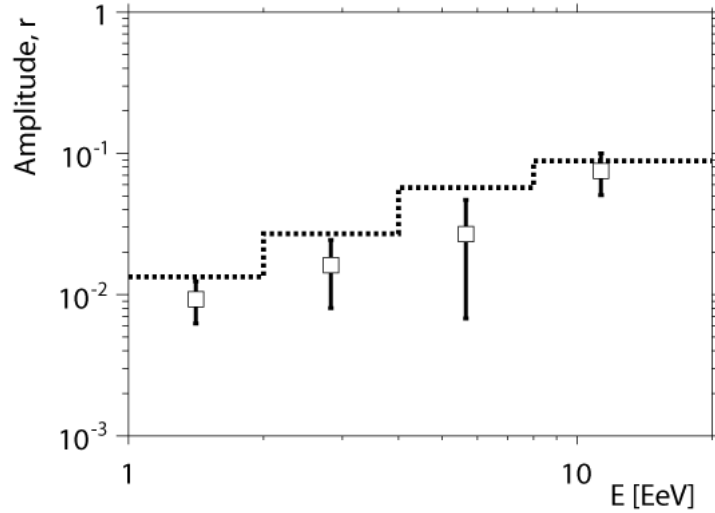
Figure 10 : Reconstructed amplitude of the dipole as a function of the energy. The dotted line stands for the 99% *C.L.* upper bounds on the amplitudes that would result from fluctuations of an isotropic distribution [68].

where $\mathbf{d}$ is the dipole unit vector. The dipole pattern is described by a declination, δ_d, a right ascension α_d, and an *amplitude r* which will give a maximum anisotropy contrast of

$$r = \frac{\Phi_{\max} - \Phi_{\min}}{\Phi_{\max} + \Phi_{\min}}. \tag{3.5.11}$$

From reference [67], estimating these three coefficients is straightforward from the estimated spherical harmonic coefficients $\overline{a}_{1m}$: $\overline{r} = [3(\overline{a}_{10}^2 + \overline{a}_{11}^2 + \overline{a}_{1-1}^2)]^{0.5}/\overline{a}_{00}$, $\overline{\delta} = \arcsin{(\sqrt{3}\overline{a}_{10}/\overline{a}_{00}\overline{r})}$, and $\overline{\alpha} = \arctan{(\overline{a}_{1-1}/\overline{a}_{11})}$. Uncertainties on $\overline{r}$, $\overline{\delta}$ and $\overline{\alpha}$ are obtained from the propagation of uncertainties on each recovered $\overline{a}_{1m}$ coefficient.

The reconstructed amplitudes $\overline{r}$ are shown in Fig. 10 as a function of the energy. The dotted line represents the 99% confidence level upper bounds on the amplitudes that would result from fluctuations of an isotropic distribution. There is no significant signal outside of statistical uncertainties. The corresponding directions as a function of energy are shown in Fig. 11 in the orthographic projection with the associated uncertainties.

In the case of independent samples whose parent distribution is isotropic, both angles are expected to be randomly distributed. In the report [65] on the first harmonic analysis, the intriguing smooth alignment of the phases in right ascension as a function of energy was pointed out and noted that such a consistency of phases in adjacent energy intervals is expected to manifest with a smaller number of events than those required for the detection of amplitudes that are significantly above the background noise in the case of a real underlying anisotropy. This motivated a prescription design aimed at establishing a 99 % confidence level whether this consistency in phases is real, using the exact same analysis as reported in [65]. The prescribed test ends once the total exposure since June 25, 2011 reaches 21,000 km^2 yr sr. Figure 12 shows the smooth fit to the data of the report [65] as a dashed line restricted to the energy range considered. It is noteworthy that though the phase between 4 and 8 EeV is poorly determined due to the corresponding direction in declination pointing close to the equatorial South Pole, a consistent smooth behavior is observed using the present analysis and applied to a data set containing two
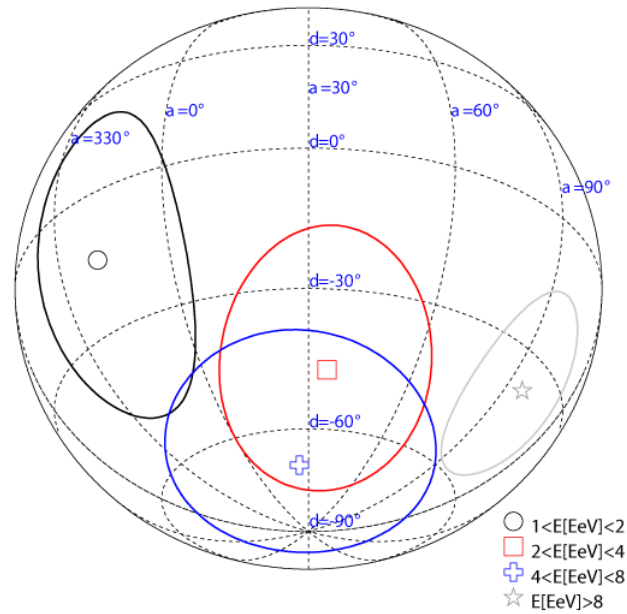
Figure 11 : Reconstructed declination and right-ascension of the dipole with corresponding uncertainties, as a function of the energy, in orthographic projection [68].
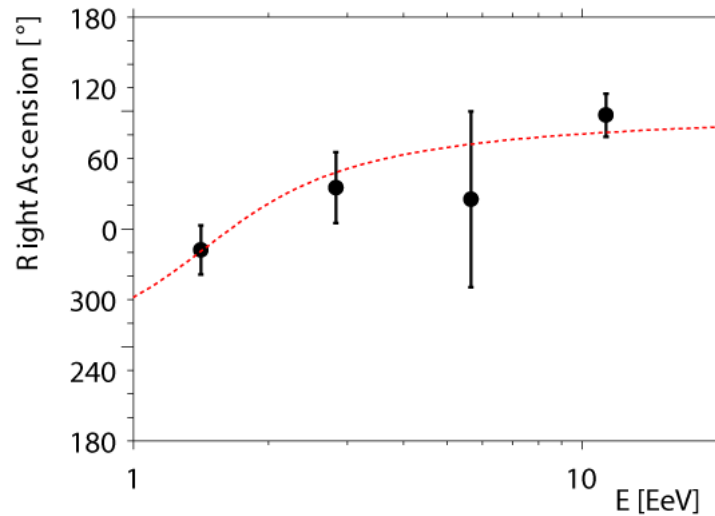
Figure 12 : Reconstructed right ascension of the dipole as a function of the energy. The smooth fit to the data of [65] is shown as the dashed line.

additional years of data [68].

3.5.3 Looking for Quadrupolar Patterns

Following again the development in reference [67], if the assumption is made that the angular distribution of cosmic rays is modulated by a dipole as well as a quadrupole, the intensity, $\Phi(\mathbf{n})$ can be parameterized in any direction $\mathbf{n}$,

$$\Phi(\mathbf{n}) = \frac{\Phi_0}{4\pi}\left(1 + r\,\mathbf{d}\cdot\mathbf{n} + \frac{1}{2}\sum_{i,j}Q_{ij}n_i n_j\right), \qquad (3.5.12)$$

Figure 13 : Amplitudes of the quadrupolar moment as a function of the energy using a multipolar reconstruction up to $\ell_{\max} = 2$. The dotted lines stand for the 99% $C.L.$ upper bounds on the amplitudes that could result from fluctuations of an isotropic distribution [68].
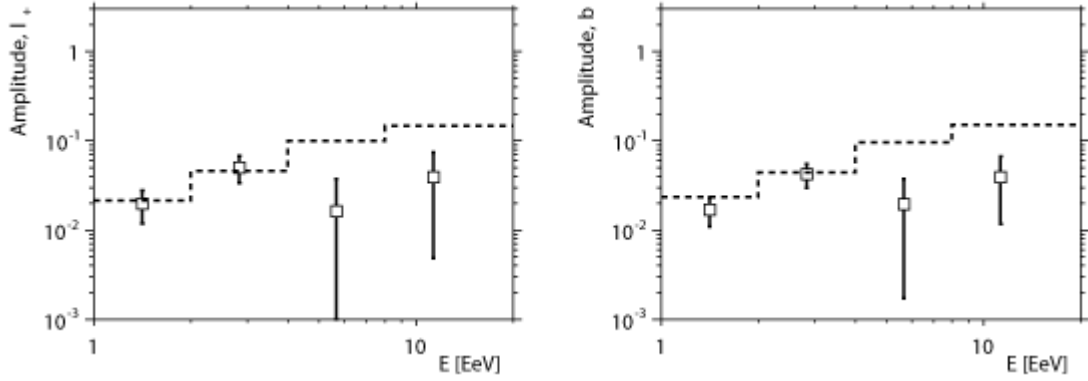
where $\mathbf{Q}$ is a traceless and symmetric second order tensor. Its five independent components are determined from the $\ell = 2$ spherical harmonic coefficients a_{2m}. Denoting the three eigenvalues of $\mathbf{Q}/2$ by $\lambda_+, \lambda_0, \lambda_-$ and the three corresponding unit eigenvectors $\mathbf{q}_+, \mathbf{q_0}, \mathbf{q}_-$, the intensity can be parameterized as,

$$\Phi(\mathbf{n}) = \frac{\Phi_0}{4\pi} \left(1 + r\, \mathbf{d} \cdot \mathbf{n} + \lambda_+(\mathbf{q}_+ \cdot \mathbf{n})^2 + \lambda_0(\mathbf{q_0} \cdot \mathbf{n})^2 + \lambda_-(\mathbf{q}_- \cdot \mathbf{n})^2 \right), \qquad (3.5.13)$$

where the quadrupole amplitude β can be defined as,

$$\beta \equiv \frac{\lambda_+ - \lambda_-}{2 + \lambda_+ + \lambda_-}. \qquad (3.5.14)$$

In absence of a dipole but in the case of a pure quadrupolar distribution, β is the standard measure of maximal anisotropy contrast,

$$r = 0 \Rightarrow \beta = \frac{\lambda_+ - \lambda_-}{2 + \lambda_+ + \lambda_-} = \frac{\Phi_{\max} - \Phi_{\min}}{\Phi_{\max} + \Phi_{\min}}. \qquad (3.5.15)$$

This means that any quadrupolar pattern can be fully appreciated by two amplitudes (β, λ_+) and three angles (δ_+, α_+) which define the orientation of $\mathbf{q}_+$ and (α_-) which defines the direction of $\mathbf{q}_-$ in the orthogonal plane to $\mathbf{q}_+$. The third eigenvector $\mathbf{q_0}$ is orthogonal to $\mathbf{q}_+$ and $\mathbf{q}_-$. Figure 13 shows the estimated amplitudes $\overline{\lambda}_+$ and $\overline{\beta}$ as function of energy. Similar to the dipolar analysis there is no evidence for anisotropy due to the 99% confidence level upper bounds on the amplitude could result from isotropic fluctuations.

3.6   Systematic Uncertainties and the Upper Limits

Small uncertainties crop up in correcting the estimator of the energy for weather and geomagnetic effect, and these propagate into systematic uncertainties in the measured anisotropy parameters. Anisotropy parameters may be altered in a systematic way by the energy dependence of the attenuation curve. These effects have been studied and quantified in the report [67] and they do not significantly change the results of the study.

The upper limits on the dipole and quadrupole amplitudes can be derived at a 99% confidence level. Figure 14 shows these while accounting for the systematic uncertainties. By
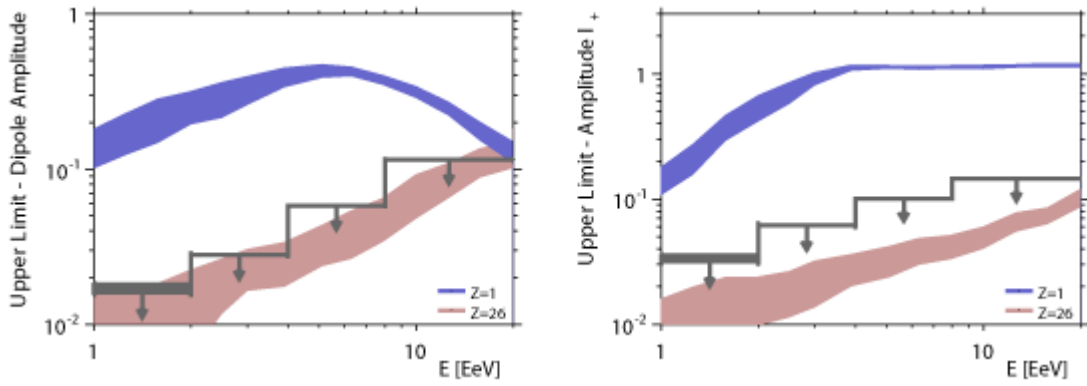
Figure 14 : 99% $C.L.$ upper limits on dipole and quadrupole amplitudes as a function of the energy. Some generic anisotropy expectations from stationary galactic sources distributed in the disk are also shown, for various assumptions on the cosmic ray composition. The fluctuations of the amplitudes due to the stochastic nature of the turbulent component of the magnetic field are sampled from different simulation data sets and are shown by the bands [68].

looking closer at the scenario in which sources of EeV cosmic rays are stationary, densely, and uniformly distributed in the Galactic disk and emit particles in all directions, the astrophysical interest can be illustrated.

The strength and structure of the Galactic magnetic field is only known approximately but obviously plays a crucial role in the propagation of cosmic rays. The Galactic magnetic field is thought to consist of a large scale regular component along with a small scale turbulent one, both having a local field strength of a few microgauss [72]. The turbulent component dominates in strength by a factor of a few but the regular component imprints a dominant drift motion as soon as the Larmor radius of cosmic rays is larger than the maximal scale of the small scale turbulences, which are thought to be in the range of 10 to 100 parsecs [68]. A recent parameterization of the regular component obtained by fitting model field geometries to Faraday rotation measures of extragalactic radio sources and polarized synchrotron emission has been adopted for the scenario [73]. A turbulent field, in addition to the regular component, is generated according to a Kolmogorov power spectrum and is pre-computed on a three dimensional grid periodically repeated in space. The size of the grid is chosen to represent the maximal scale of the turbulences or 100 pc. The strength of the turbulent component is taken as three times of that of the regular one. In order to describe the propagation of the cosmic rays from their sources with energies $E \geq 1$ EeV in this field, the direct integration of the trajectories is the most appropriate tool [68]. To get the anisotropy of cosmic rays emitted from sources uniformly distributed in a cylinder with a radius of 20 kpc from the galactic center and with a height of $\pm$ 100 pc, a method that consists in back-tracking anti-particles with random directions from the Earth to outside the Galaxy [68]. Each test particle probes the total luminosity along the path of propagation from each direction as seen from the Earth. Stationary sources that emit cosmic rays in all directions are expected to have flux in the initial sample direction proportional to the time spent by each test particle in the source region [68].

Anisotropic amplitudes, of course, depend on the rigidity E/Z of the cosmic rays, where Z represents the electric charge of the particles. In order to illustrate the upper limits two extreme

single primaries are considered: protons and iron nuclei. This method is useful to probe the allowed contribution of each primary as a function of energy.

Figure 14 shows the dipole and quadrupole amplitudes obtained for several energy values with the range of $1 \leq E/\mathrm{EeV} \leq 20$. To probe unambiguously amplitudes down to the percent level, it is required to generate simulated event sets with at least $\simeq 5 \ 10^5$ test particles. This large of a number of simulated events shrinks the statistical uncertainties on amplitudes at the 0.5% level [68]. There is an intrinsic variance in the model for each anisotropy parameter due to the stochastic nature of the turbulent component of the field. This is estimated through simulating 20 sets of 5×10^5 test particles, where the configuration of the turbulent component is frozen in each set. The RMS values of the amplitudes sampled in this fashion is shown using the bands in Fig. 14.

The amplitudes that result for proton primaries largely stand about the allowed limits. So, unless the strength of the Galactic magnetic field is much higher than what was used in this scenario, the upper limits derived exclude that the light component of cosmic rays comes from Galactic stationary sources densely distributed in the Galactic disk and emitting in all directions. The dipole limits below the ankle energy require that the fraction of protons should not exceed $\simeq 10\%$ of the cosmic ray composition. This is of interest in the view of the indications for the presence of a light component around 1 EeV from shower depth maximum measurements [46, 47, 74]. Firm interpretations of these measurements in terms of atomic mass still suffer from some ambiguity due to the uncertain hadronic interaction models used to describe the shower developments. If, however, the cosmic ray composition around 1 EeV results are from a mixture containing heavy primaries of galactic origin and light primaries of extragalactic origins then the upper limits can be respected. This is because large scale anisotropy amplitudes below the percent level are expected for extragalactic cosmic rays, due to the motion of the Galaxy relative to a possibly stationary extragalactic cosmic ray rest frame [64, 75].
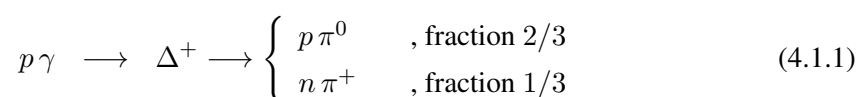
Chapter 4

Galactic Neutron Astronomy

4.1 General Idea

In cosmic ray anisotropy studies, magnetic fields are the great eraser, showing us the results of the extreme environments that surround sources and accelerate particles to almost unimaginable energies. However, the magnetic fields inherent to the galaxy and the Earth itself erase any information about where these sources are located. This is of course because the majority of studies have historically focused on protons and other charged nuclear fragments, Z, which are greatly affected by ambient magnetic fields, which leads to the overall isotropic appearance of the cosmic ray sky below energies of 10^{18} eV. At energies above 10^{19} eV charged cosmic rays should no longer be bound by the galactic magnetic field and since there does not appear to be any strong correlation with the detection of these events and the galactic plane is it naturally assumed that these UHECRs are produced extragalactically. However, neutrons at energies around 10^{18} eV produced at the source have the ability to escape deflection on magnetic fields [76–78]. At the high end of the spectrum neutrons nay also survive the trip to Earth from the nearest radiogalaxy Centaurus A [79, 80]. This opens the door to surveying galactic (and nearby extragalactic) sources of UHECR neutrons.

Neutrons are not bent by Galactic or extra-galactic magnetic fields and should point to their sources. For this reason, neutrons cannot be trapped inside the shock fronts which are assumed to accelerate UHECRs. This means that they need to get their high energies through some other mechanism. Within the astrophysical source UHE neutrons are produced most efficiently by pp collisions. Inelastic pp collisions lead to roughly equal numbers of π^0's, π^+s, and π's, with a 50% chance of neutron production [81]. Two other possible sources for UHE neutron production, albeit less effective, are the disassociation of heavy ions into their constitute components [82] as well as charge exchange through $p\gamma$ interactions

$$p\gamma \; \longrightarrow \; \Delta^+ \longrightarrow \begin{cases} p\,\pi^0 & \text{, fraction 2/3} \\ n\,\pi^+ & \text{, fraction 1/3} \end{cases} \tag{4.1.1}$$

Once the UHE neutrons are produced they travel in straight lines away from the source and when impacting the atmosphere produce air showers that are identical to those produced by protons. UHE neutrons coming from a point-like source would appear as an excess number of

events around a certain direction in the sky. This source of directional information is not without its own drawbacks of course. Free neutrons are unstable and undergo beta decay with a mean lifetime of 886 seconds, τ_n, when at rest [83]. This means that UHE neutrons can only travel a limited distance. To find that distance we can use Special Relativity with the Lorentz factor given by $\gamma_n \equiv E_n/m_n$,

$$d_n(E_n) = c\gamma_n\tau_n \simeq 9.2 \left(\frac{E_n}{\text{EeV}}\right) \text{kpc}. \tag{4.1.2}$$

From this equation it is easy to see that neutrons with an energy of approximately 10^{18} eV, or 1 EeV can travel about 9.2 kpc. A possible source of UHECRs, the Galactic Center, is only about 8.3 kpc from Earth. If we increase the energy of neutrons to 2 EeV or greater the travel distance can encompass the entire Galaxy, for which the radius is is about 15 kpc. Therefore any sources within 9.2 kpc, such as the Galactic Center or the Cygnus spiral arm, should be detectable for neutrons within the 1 EeV range and all Galactic sources should be detectable for neutrons $E_n \geq 2$ EeV.

Continuing to build the case for the search for UHE neutrons if we look back at Eq. 4.1.1 we see that as previously stated neutrons are produced by a charge exchange interactions in which the neutron acquires the lion's share of the initial proton energy. Thus because only a small fraction of energy goes into photon production neutron production should exceed the hadronic production of photons that have the same energy assuming that the accelerated proton spectrum falls approximately by $1/E^2$ [40]. Then based on the energy flux of TeV gamma rays, which is in excess of 1 eV/cm^2/s at Earth for some Galactic sources [84], neutron fluxes from known sources should be detectable at the Pierre Auger Observatory [40]. If the gamma rays are coming from π^0 meson decay then a source with a $1/E^2$ differential energy spectrum, which puts equal energy into each decade, then such sources could also be feasibly producing EeV photons as well. The flux of these EeV photons should also exceed the 1 eV/cm^2/s of the TeV gamma rays at Earth.

4.2 Blind Search Methods

4.2.1 Data Set

The data set used in this study for the blind search of the southern sky consists of the Pierre Auger Observatory SD events that were recorded from January 1, 2004 to September 30, 2011. This period of time saw the SD array grow from 154 stations to 1660 stations. For the analysis events were restricted to having a zenith angle less than $60°$ and was only accepted if all six of the nearest neighbors to the detector with the highest signal were active as the time of the event. This is the standard geometrical aperture cut that ensures a good event reconstruction [21]. When eliminating times when the SD array was unstable the total exposure with these cuts is 24,880 km^2 sr yr for the period of time analyzed, leading to 429,138 events with $E \geq 1$ EeV [40].

Table 1 : Energy cuts for neutron searches.

Energy Range	Neutron Travel Distance	Events
$E \geq 1$ EeV	$d_n \gtrsim 9.2$ kpc	429,138
1 EeV $\leq E < 2$ EeV	9.2 kpc $\lesssim d_n \lesssim 18.4$ kpc	319,818
2 EeV $\leq E < 3$ EeV	18.4 kpc $\lesssim d_n \lesssim 27.6$ kpc	61,059
$E \geq 3$ EeV	$d_n \gtrsim 27.6$ kpc	48,261

4.2.2 Energy Cuts

Four energy ranges were used for the blind search of the Pierre Auger Observatory data set and for upper limit analysis, which are given in Table 1. The first energy range is a cumulative data set that should be able to give the maximized sensitivity to a flux that extends over the entire range of energies represented by the latter three independent data sets. Splitting up the energies ranges allows for the survey of possible more distant sources, from the higher energy ranges, as well as possibly nearby sources which are strongly favored in the lower-energy regime.

4.2.3 Simulation Data Sets

The use of simulated data sets allows us to compare any possible excess of events in any solid angle target with the number of events that would have been within the solid angle target had the neutral flux been non-existent. The baseline for the expected number of events is taken to be the mean number found in 10,000 simulated events data sets which were obtained using actual arrival directions for each energy range. Each of these simulated data sets will use the same number of arrival directions as the actual data set. The process uses a scrambling procedure that carefully smooths out any inherent small scale anisotropies. The simulated arrival direction is produced by randomly sampling a sidereal time and a zenith angle from a set of measure values as well as an azimuthal angle from a uniform distribution over 2π radians. Thus each simulated data set should be equivalent to the actual data observed except for statistical fluctuations, unless there are astrophysical fluxes that have imprinted small scale anisotropies within the actual data [40].

The expected number of events per solid angle target, averaging over the targets with centers in 3-degree declination bands is shown in Fig. 15. The expected number for each energy range depends on declination somewhat because of the target size's declination dependence but mostly because the directional exposure varies with the declination.

4.2.4 Li-Ma Significance

Careful analysis of the actual observed data is required to determine the probability that an excess number of events is due to a genuine small scale anisotropy, such as a point-like source, rather than an apocryphal background fluctuation. Using the formulation by Li and Ma [85], which was originally developed to study sources of γ-rays, we can assume that a detector points in the direction of a suspected source for a certain amount of time, t_{on}, and counts N_{on} events.
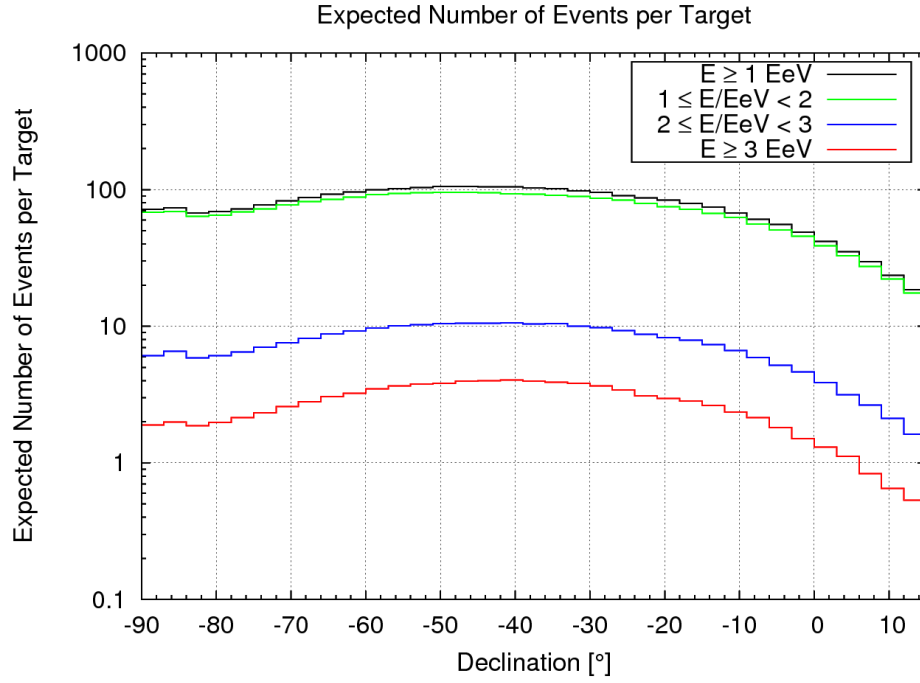
Figure 15 : The expected number of events per target for each of the four energy ranges, averaged in 3-degree bands of declination [40].

Then the detector looks only at the background or for a baseline measurement without any sources for a time t_{off} and counts N_{off} events. At this point we can define a quantity, α or the Li-Ma parameter, as the ratio of the on-source time to the off-source time, $\alpha = t_{\text{on}}/t_{\text{off}}$. See Fig. 16 for a graphical representation.

It is possible to then find the signal by subtracting the background events, $\hat{N}_B$, that make up part of the N_{on} events.

$$\hat{N}_B = \alpha N_{\text{off}} \tag{4.2.1}$$

then the observed signal,

$$N_S = N_{\text{on}} - \hat{N}_B = N_{\text{on}} - \alpha N_{\text{off}} . \tag{4.2.2}$$

The problem, of course, is that the excess events, $N_{\text{on}} - \hat{N}_B$, could have been the result of a statistical fluctuation in the background, being that, it is not known exactly and can only be extrapolated. We can test the statistical significance, S, of an observation, however, by looking at the standard deviation of the observed signal N_S.

Because the event counts N_{on} and N_{off} are based on independent measurements the variance of the signal N_S is,

$$\sigma^2(N_S) = \sigma^2(N_{\text{on}}) + \sigma^2(\alpha N_{\text{off}}) = \sigma^2(N_{\text{on}}) + \alpha^2 \, \sigma^2(N_{\text{off}}) \tag{4.2.3}$$

and thus an estimate of the standard deviation is found to be,

$$\hat{\sigma}(N_S) = \sqrt{\hat{\sigma}^2(N_{\text{on}}) + \hat{\sigma}^2(\alpha N_{\text{off}})} = \sqrt{N_{\text{on}} + \alpha^2 N_{\text{off}}} \tag{4.2.4}$$

Then defining the significance, S, as the ratio of the excess events above the background to its
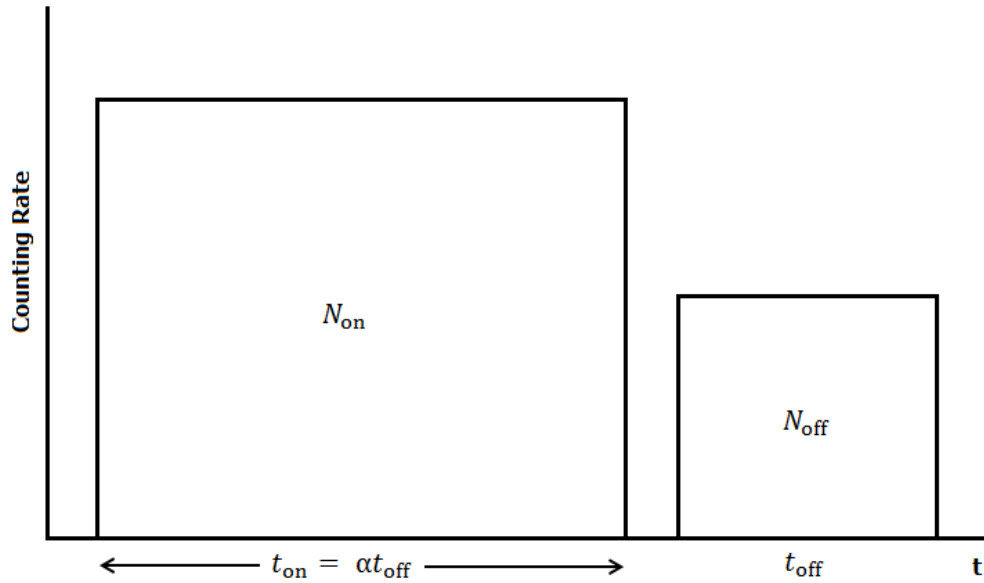
Figure 16 : A graphical comparison of the counting rates from [85]

standard deviation,

$$S = \frac{N_S}{\hat{\sigma}(N_S)} = \frac{N_{\mathrm{on}} - \alpha N_{\mathrm{off}}}{\sqrt{N_{\mathrm{on}} + \alpha^2 N_{\mathrm{off}}}} \tag{4.2.5}$$

This equation is just the Poisson law of the events in N_{on} and N_{off} [86].

4.2.5 Upper Limit Calculation

There are multiple ways of defining the upper limit, s_{UL}, of a confidence level, CL, for an expected signal, s, results in a count of n observations while in the presence of a Poisson background of mean value, b. The definition chosen for s_{UL} in the blind search is that of Zech [87] which uses a fractional confidence level, CL (e.g. 95% confidence level $\Rightarrow CL = 0.95$ and $1 - CL = 0.05$),

$$P(\leq n|b + s_{\mathrm{UL}}) = (1 - CL) \times P(\leq n|b). \tag{4.2.6}$$

This definition was chosen over the classical definition because it avoids unphysical negative upper limits when the observed number is a strong downward fluctuation of the background. Equation 4.2.6 can be interpreted from a frequentist viewpoint as "an infinitely large number of repeated experiments looking for a signal with expectation s_{UL} and background with mean b, where the background contribution is restricted to a value less than or equal to n, the frequency of observing n or fewer events is α" [87]. In the case of a Poisson distribution this definition for the upper limit agrees with the Bayesian upper limit when taking a flat prior probability distribution:

$$\int_0^{s_{UL}} P(n|b + s)ds = (CL) \int_0^\infty P(n|b + s)ds. \tag{4.2.7}$$

The upper limit,s_{UL}, in this equation is for the expected number of events from a source that would be contained within the top-hat target region defined by the angular resolution.

4.2.6 Flux Upper Limit

Taking the upper limit on the number of events as described in 4.2.5 and dividing it by the *directional exposure* at the target center, we can get the *flux upper limit*. The exposure is dependent on the trigger efficiency which is 100% for events with energies above 3 EeV [37] but below this energy the efficiency can depend on event energy, the zenith angle, and the mass of the primary. The directional exposure, measured in km^{2}yr, for any celestial direction is given by $\frac{b}{\omega I}$, where b is the expected number that is found empirically from the average of simulated data sets within the target solid angle, ω, and I is the cosmic ray intensity with units given by (km^2 sr yr)$^{-1}$. The intensity is calculated by integrating the know energy spectrum [42] over the relevant energy range. In Fig. 17 the dependence of the directional exposure on the declination is shown for four different energy ranges.
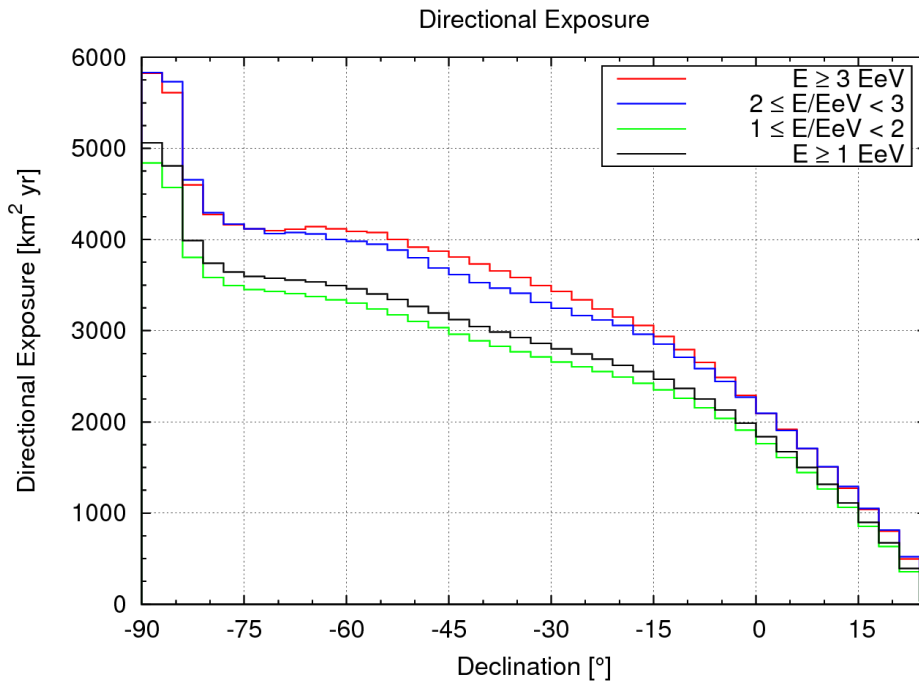

Figure 17 : The directional exposure for each of the four energy ranges, averaged in 3-degree bands of declination [40].

4.2.7 Pixelation and Target Spacing

Directional exposure quickly falls for the Pierre Auger Observatory SD array for declinations close to $+25°$, which is the maximum declination that can be observed at $-35°$ latitude with a zenith angle less than $60°$. By limiting the search for point-like sources to regions where the directional exposure is greater than 1000 km^{2}yr, by keeping declinations below $+15°$, large statistical fluctuations can be avoided.

To produce the observed and expected celestial maps the Hierarchical Equal Area iso-Latitude Pixelization (HEALPix) data structure was used. HEALPix uses a library of computational algorithms and visualization software to create discretized spherical maps from astronomical data [88]. Locations on these spheres are defined by $z \equiv \cos\theta, \phi$ where $\theta \in [0, \pi]$ is

the colatitude in radians measured from the North Pole and $\phi \in [0, \pi]$ is the longitude in radians measured eastward. For the resolution parameter N_{side} the pixels are laid out on $4N_{\text{side}} - 1$ iso-latitude rings and are ordered using a pixel index $p \in [0, N_{\text{pix}}]$ running around those rings from north to south. Here $N_{\text{pix}} = 12N_{\text{side}}^2$ is the total number of base-resolution pixels made up of the number of pixel layers between the North and South Poles and the number of circum-polar pixels. Pixel centers can be located on each hemisphere using a series of index equations [88].

For the blind search the target centers, with a $0.6°$ separation, were taken as the central points of the HEALPix grid with $N_{\text{side}} = 128$. Since the target diameters are significantly larger than the $0.6°$ separation there is a strong overlap and are not considered statistically independent trials. However, this is necessary to avoid the failure to detect a neutron flux because it was divided between two ir more adjacent targets.

To aide computational efficiency a finer pixelation, $N_{\text{side}} = 512$ is used to store and count events. The targets are made up of a union of small pixels whose centers are within the target radius, rather than being perfect circles. There are, on average, 342 small pixels in the targets that are used for the energy ranges going down to 1 EeV and 106 small pixels, on average, in the smaller targets used for E > 3 EeV. Actual and simulated data sets are summarized by the counts of events in the small pixels and the number of events per target is the sum of the counts in its constituent pixels.

4.3 Statistical and Systematic Uncertainties

The number of events in each target represents some statistical uncertainty which stems from Poisson fluctuations. However, the Li-Ma significance and the flux upper limits at a fixed confidence level are designed to take into account the statistical Poisson fluctuations, thus these fluctuations are not a concern.

The mean particle upper limit scales approximately with the square root of the expected number, b, in the target. This can lead to a systematic error in the angular resolution since the upper limit is therefore proportional to the target radius or the assumed angular resolution. There is a 10% systematic uncertainty in the angular resolution for each energy bin. A genuine signal would also be under or overestimated if measured within a fixed target radius proportional to an assumed angular resolution that is to small or large respectively. The top-hat measurement produces a fractional error as well of 0.714 times the fractional error in the angular resolution, so a 10% uncertainty in the angular resolution will equate to a 7% uncertainty due to the top-hat measurement [40].

It is possible that errors could be found in the expected background counts due to imperfections in the smoothing procedure based on simulated data sets. These uncertainties should be quite small and have a negligible impact on the results especially when compared to Poisson fluctuations throughout the sky and for all energy ranges. Using alternative methods to obtain the background baseline give nearly identical results. Likewise, there could also be some uncertainties due to the way the Li-Ma parameter, α, was identified but the Li-Ma significances remain stable as long as α remains small. The results for the blind search would have been

the same for alternative identifications of α which again implies insignificant uncertainty in the background counts [40].

While the results are presented for fixed energy ranges if there is a systematic error in the energy normalization then the Li-Ma significance and the flux upper limit for each target pertain to a different true energy range. The Pierre Auger Observatory scale currently has a systematic uncertainty of about 22% [42]. Also, as previously noted the SD is not 100% efficient for energies below 3 EeV. This trigger inefficiency can produce a systematic energy error by favoring an upward fluctuation in signals in the surface stations. Events that have been measured in the hybrid mode by taking advantage of the FD and SD indicate that the SD energy assignments are systematically high by about 2% for 2-3 EeV and close to 7% for 1-3 EeV events [40].

Fluctuations in the energy measurements can also cause an unequal migration of signal and background events into and out of an energy range. This migration will affect the apparent signals and upper limits. The effect is dependent on the exact shape of the arriving neutron signal spectrum which includes its suppression at low energies due to in-flight decays. A significant underestimation in the upper limit could exist if there were no arriving neutrons to spill upward into an energy bin which does not gain background events by upward energy measurement fluctuations. These errors are not very large since the energy measurement fluctuations are small in comparison to the energy ranges and the background contamination from another outside energy range does not exceed more than a few percent.

Uncertainty in the cosmic ray composition also leads to some systematic uncertainty. There is solid evidence for a mixed cosmic ray composition which includes protons throughout the EeV energy decade [46]. As mentioned in the beginning of the chapter neutron showers are reconstructed the same as showers produced by protons. If heavy nuclei alone made up the composition the limits would pertain to somewhat higher neutron energies than stated. However, for a composition that consists of a substantial proton component the energies reconstructed for neutron showers based on SD data do not systematically differ more than 5% from the background cosmic ray energies which are calibrated by using air fluorescence measurements [40].

4.4 Results for the Blind Search

4.4.1 Li-Ma Significances

Fig. 18 shows the statistical results for the ensemble of celestial targets. The red lines in the figure show the distribution of Li-Ma significance obtained from the data and the blue lines show the expectation obtained by averaging over the simulated data sets. The simulated data sets were analyzed in exactly the same way as the real data using all of the other simulation data sets to determine the background for every target. The figure also shows the Gaussian function that the Li-Ma distribution is expected to approximate if deviations from expected values are due only to statistical fluctuations.

Two plots exist for each energy range in Fig. 18. On the left side of the figure is the differential histogram binned in increments of Li-Ma significance. The right hand side are two unbinned integral distributions of the same Li-Ma significances. One of these focuses on the
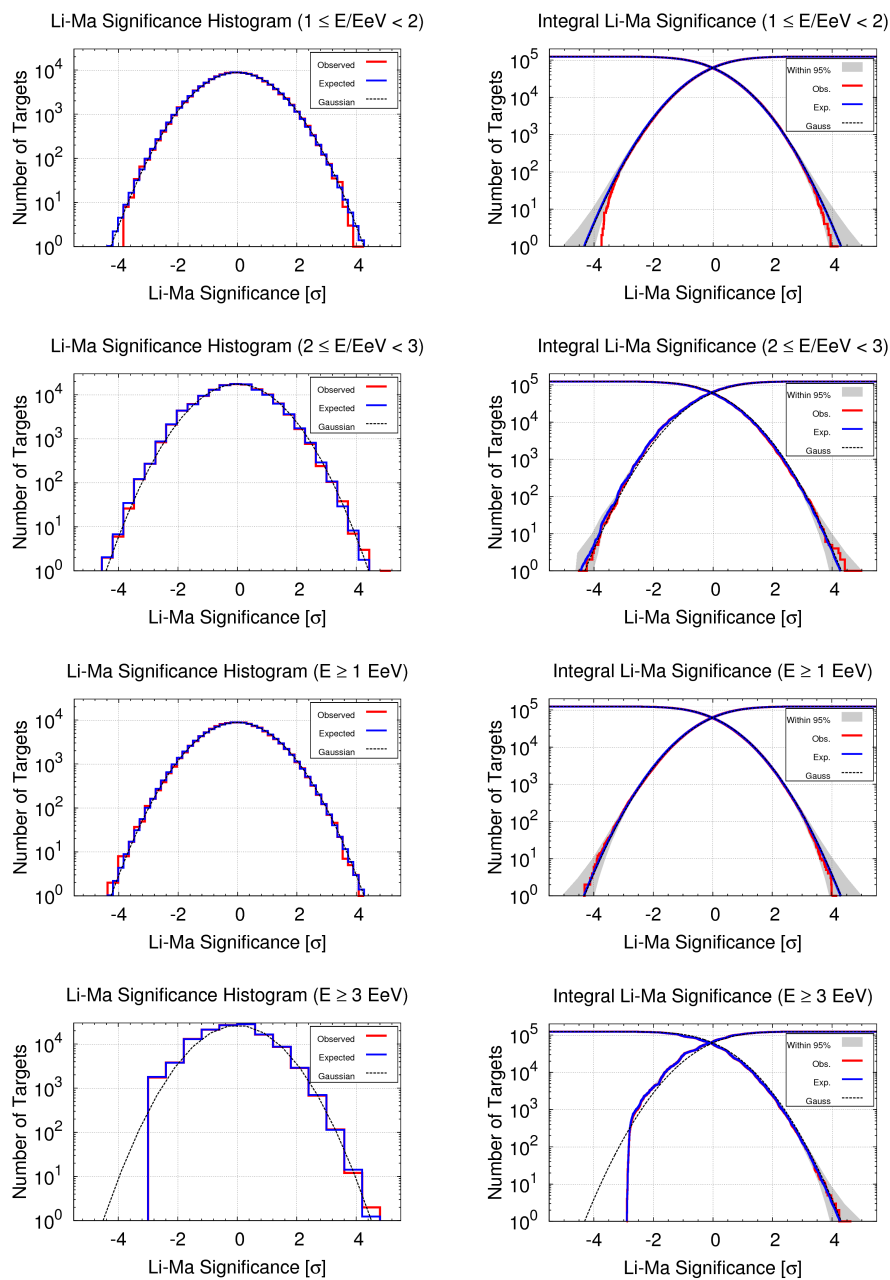
Figure 18 : Differential distributions (left) and integral distributions (right) of Li-Ma significance for the four energy cuts (1-2, 2-3, ≥ 1, and ≥ 3 EeV). Results for real data are shown by red curves. Expectations from simulation data sets are blue curves. Shaded regions are 95% containment of results of simulated data sets. Dashed curves are Gaussian approximations for the expected Li-Ma distribution. [40].

tail of high significance by plotting for each Li-Ma significance the total number of targets of equal or greater significance. The other one focuses on the tail of low significances by plotting the total number of targets that had equal of lower Li-Ma significance. The shaded bands in the figure represent 95% containment bands for simulation data sets. 2.5% if the simulation integral curves were to the left or right on the band.

As the red curve does not lie to the right of the right-hand shaded region means that this search did not result in identifying obviously significant hot spots. The deviation from the Gaussian curve for negative significances for energies $E \geq 3$ EeV is the result of very low statistics in many targets [40].

4.4.2 Upper Limits

The color sky plots in Fig. 19 display the flux upper limits at a 95% confidence level for each target direction. These limits were found by using the methods previously describing in sections 4.2.5 and 4.2.6.
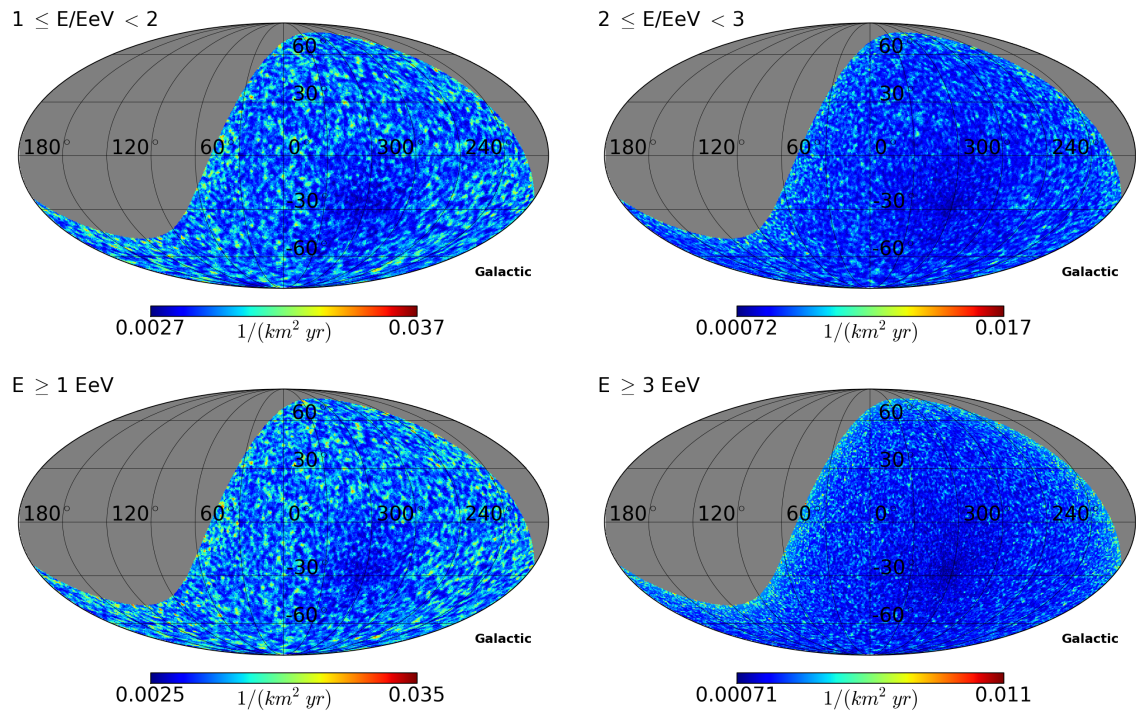

Figure 19 : Celestial maps of the flux upper limit ($\frac{\text{particles}}{\text{km}^2 \text{yr}}$) in Galactic coordinates [40].

In Fig. 20 the mean flux upper limit is shown as a function of the declination for each of the energy ranges. For the northern declinations, where the directional exposure is reduced, the upper limits tend to be greater (weaker). The limits are the lowest (strongest) near the south pole (-90°) where the declination exposure is maximum but the mean value is less accurately determined in that region because there are relatively few targets in a declination band [40].
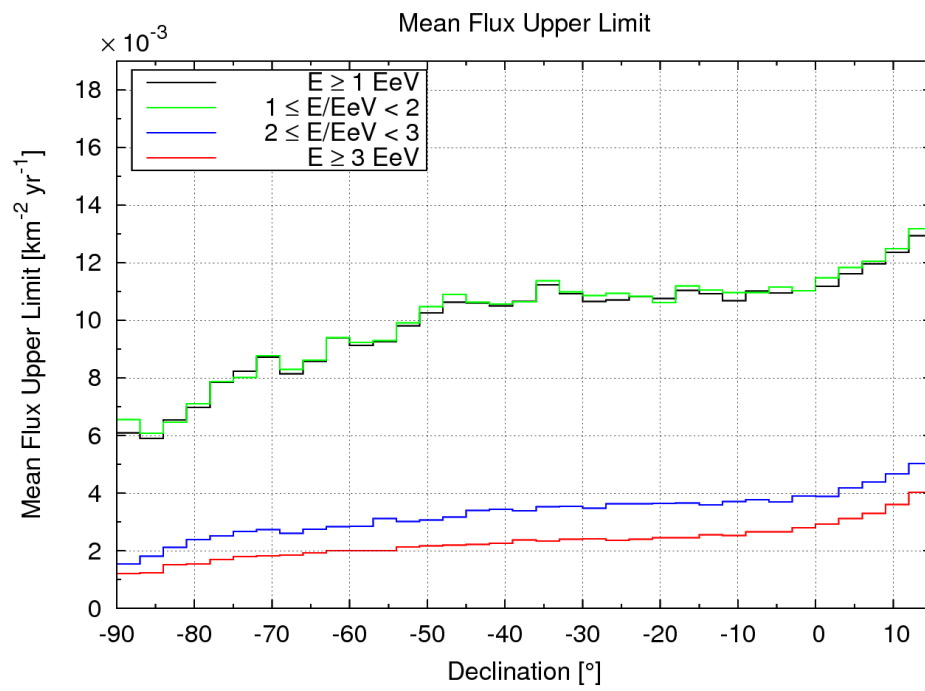
Figure 20 : The flux upper limit for each of the four energy ranges, averaged over targets in 3-degree bands of declination [40].

Chapter 5

Quest for Cosmic Neutrino Sources

5.1 General Idea

In the context of multimessenger approaches to searching from cosmic ray sources, the neutrino plays an important role. As stated in Sec. 1.3, neutrinos, created by protons interacting with a photon field or other protons, when detected at high energies ($>$ 100 TeV), permit an exploration of the region of acceleration. UHEνs emerge from the acceleration region and propagate throughout the cosmos remaining essentially unaffected by magnetic fields or dust clouds. This implicit advantage in travel also manifests itself in our ability to detect them unfortunately [89–93].

Despite this detection challenge, the observation of UHECRs make the presence of UHEνs very probable. This is due to all UHECR models predicting neutrinos from the decay of charged pions coming from proton-proton or proton-photon interactions within the sources themselves, so called "astrophysical" neutrinos, and/or with background radiation fields throughout the cosmos, "cosmogenic" neutrinos [94, 95]. One of the background radiation fields that supplies photons for ultra-high energy proton-photon interactions is the CMB. With these UHECR models there are large uncertainties in the neutrino flux which stem from the UHECR spectrum and on the spatial distribution and evolution of the sources [96–102]. For example, if the majority of UHECRs are heavy nuclei then the incoming UHEν amount would be strongly suppressed [103, 104].

There is a lot of excitement surrounding the possibility of observing of UHEν and rightfully so. UHEνs would open new windows of opportunity to study the Universe. Unperturbed by magnetic fields and able to travel through dust clouds, neutrinos would reveal regions previously unexplored. Tracing the neutrinos back to their source would give information that would shed light on the origin of cosmic rays and give a greater understanding of the GeV-TeV gamma-ray production mechanism [105, 106].

The Pierre Auger Observatory was originally designed to measure UHECR EAS. However, the surface detector array can also be used to identify UHEνs [107]. All flavors (electron, muon, and tau) of neutrinos are able to interact with the atmosphere at various depths through weak force interactions via charged or neutral currents thus inducing a "downward-going" (DG) shower. Although tau neutrinos may not be produced within the source itself, due to neutrino

oscillations over cosmological distances, equal fluxes for each flavor are expected to arrive at the Earth. Tau neutrinos are also able to go through charged current interactions by traveling through the Earth's crust. From this interaction a tau lepton is produced and after emerging from the surface of the Earth and decaying in the atmosphere, will set off an "Earth-Skimming" (ES) upward-going shower.

Due to a background of events flooded with standard UHECRs (protons and nuclei) and photons to a smaller extent, identifying candidate neutrino events presents a challenge. Highly inclined (zenith angle $\theta > 75°$) *ES* and *DG* neutrino-induced showers will present a large electromagnetic component at the ground, so called "young showers." These young showers produce signals spread over hundreds of nanoseconds in several of the triggered SD stations. In contrary so-called "old showers" initiated by standard UHECRs are dominated by muons at the ground level, with signals typically spread over only tens of nanoseconds.

The ability to discriminate between these young and old showers, and therefore between standard UHECRs and UHEνs, is made possible from fast sampling (25 ns) of the SD digital electronics which is sensitive to several observables that depend on time structure. Candidate UHEνs are searched for in inclined showers in the ranges $75° < \theta < 90°$ and $90° < \theta < 96°$ for the *DG* and *ES* analysis, respectively [108].

5.2 Astrophysical and Cosmogenic Neutrino Production

As previously mentioned, there are two primary types of UHEνs that can arrive at Earth, astrophysical and cosmogenic. Astrophysical neutrinos are those that have been produced via proton-proton and/or proton-photon interactions within shock fronts located at the source itself. Within potential astrophysical sources of UHEνs there are also neutrons that can interact in a similar fashion rather than protons. This neutron interaction will lead to π^- particles. If energies are high enough kaons will also begin attributing to the spectrum.

Charged pions produced in the interactions of protons, neutrons, and kaons decay to produce neutrinos,

$$\pi^+ \to \mu^+ \, \nu_\mu \quad \to \quad e^+ \, \nu_e \, \overline{\nu}_\mu \, \nu_\mu$$
$$\pi^- \to \mu^- \, \overline{\nu}_\mu \quad \to \quad e^- \, \overline{\nu}_e \, \nu_\mu \, \overline{\nu}_\mu \, .$$

The existence of comsogenic neutrinos is implied by the prediction of the GZK cutoff at the highest energies of the UHECRs spectrum due to proton interactions with the CMB via;

$$p \, \gamma_{CMB} \to \begin{cases} \Delta^+ \\ p \, e^+ \, e^- \, , \end{cases} \tag{5.2.1}$$

and then neutrinos are produced during the decay of the Δ-resonance into pions,

$$\Delta^+ \longrightarrow \begin{cases} p \, \pi^0 & \text{fraction } 2/3 \\ n \, \pi^+ & \text{fraction } 1/3. \end{cases} \tag{5.2.2}$$

The resulting diffuse flux of cosmogenic or GZK neutrinos ranges from approximately $E_\nu \sim 10^{16}$ eV to $E_\nu \sim 10^{21}$ eV [96–102].

5.3 Neutrino Oscillations

One of neutrinos unique properties is its ability to oscillate between flavors. It is because of this oscillation that equal number of electron, muon, and tau neutrinos are expected to arrive at Earth. Within the source, if we assume that equal numbers of positively and negatively charged pions are produced and that no tau neutrinos are produced in the initial pion decay then the flavor ratio for the neutrinos produced is

$$(\nu_e : \nu_\mu : \nu_\tau) = (\overline{\nu}_e : \overline{\nu}_\mu : \overline{\nu}_\tau) = (1 : 2 : 0). \tag{5.3.1}$$

The oscillation of flavors occurs because neutrinos have mass eigenvalues that do not vanish and mass eigenstates, $|\nu_j>$, $j = 1, 2, 3$, are intermixed with the flavor eigenstates, $|\nu_\alpha>$, $\alpha = e, \mu, \tau$, by way of

$$|\nu_\alpha(t)> = \sum_{j=1,2,3} U_{\alpha j} \exp(-i\, E_j t)|\nu_j>, \tag{5.3.2}$$

where E_j is the energy of the mass eigenstate j. Depending on angles θ_{12}, θ_{13}, and θ_{23}, and a phase δ the neutrino mixing matrix or *PMNS matrix* ($U_{\alpha j}$) can be given as

$$U = \begin{pmatrix} c_{12}\, c_{13} & s_{12}\, c_{13} & s_{13}\, e^{-i\delta} \\ -s_{12}\, c_{23} - c_{12}\, s_{23}\, s_{13}\, e^{i\delta} & c_{12}\, c_{23} - s_{12} s_{23} s_{13} e^{i\delta} & s_{23}\, c_{13} \\ s_{12}\, s_{23} - c_{12}\, c_{23}\, s_{13} e^{i\delta} & -c_{12}\, s_{23} - s_{12}\, c_{23}\, s_{13} e^{i\delta} & c_{23}\, c_{13} \end{pmatrix}, \tag{5.3.3}$$

where $c_{jk} := \cos(\theta_{jk})$ and $s_{jk} := \sin(\theta_{jk})$, $j = 1, 2$ and $k = 1, 2, 3$ represent the angle dependence. Using values from solar, atmospheric, and beamline neutrinos [109–111]

$$\theta_{12} \approx \pi/6 \tag{5.3.4}$$

$$\theta_{23} \approx \pi/4 \tag{5.3.5}$$

$$\theta_{13} \approx 0 \tag{5.3.6}$$

the matrix becomes,

$$U = \begin{pmatrix} \frac{\sqrt{3}}{2} & \frac{1}{2} & 0 \\ -\frac{1}{2\sqrt{2}} & \frac{\sqrt{3}}{2\sqrt{2}} & \frac{1}{\sqrt{2}} \\ \frac{1}{2\sqrt{2}} & -\frac{\sqrt{3}}{2\sqrt{2}} & \frac{1}{\sqrt{2}} \end{pmatrix}. \tag{5.3.7}$$

The probability for neutrinos to oscillate between flavor states starting from the emission of the neutrino at the source is written as,

$$P_{\nu_\alpha \to \nu_\beta} = |<\nu_\beta(t)|\nu_\alpha(t=0)>|^2 \tag{5.3.8}$$

$$= \delta_{\alpha\beta} - 4 \sum_{j>i} U_{\alpha i}\, U_{\beta i}\, U_{\alpha j}\, U_{\beta j} \sin^2\left(\frac{\delta m_{ij}^2\, L}{4}\right) \tag{5.3.9}$$

where α and β represent the different flavor states. From the previous results the probability for a neutrino flavor of ($\nu_e^{source}, \nu_\mu^{source}, \nu_\tau^{source}$) changing to a flavor vector ($\nu_e^{Earth}, \nu_\mu^{Earth}, \nu_\tau^{Earth}$) is

$$\begin{pmatrix} \nu_e^{source} \\ \nu_\mu^{source} \\ \nu_\tau^{source} \end{pmatrix} = \frac{1}{18} \cdot \begin{pmatrix} 10 & 4 & 4 \\ 4 & 7 & 7 \\ 4 & 7 & 7 \end{pmatrix} \cdot \begin{pmatrix} \nu_e^{Earth} \\ \nu_\mu^{Earth} \\ \nu_\tau^{Earth} \end{pmatrix}. \tag{5.3.10}$$
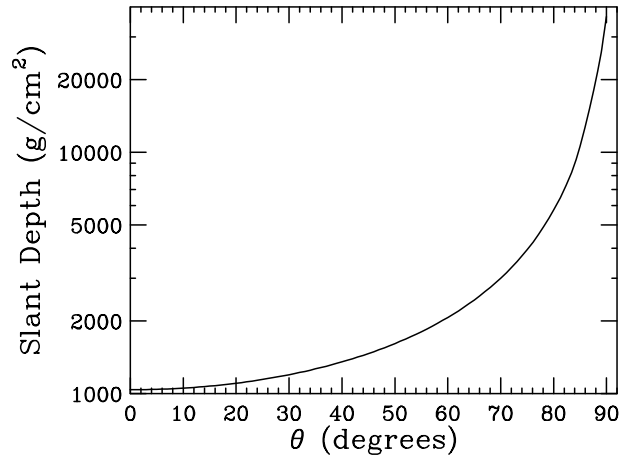
Figure 21 : Slant depths corresponding to various zenith angles θ considering the curvature of the Earth [11]

Referring back to our original assumption of the flavor ratio produced at the source,

$$\begin{pmatrix} \nu_e^{source} \\ \nu_\mu^{source} \\ \nu_\tau^{source} \end{pmatrix} = \begin{pmatrix} 1 \\ 2 \\ 0 \end{pmatrix}. \tag{5.3.11}$$

Then the final flavor vector becomes

$$\begin{pmatrix} \nu_e^{Earth} \\ \nu_\mu^{Earth} \\ \nu_\tau^{Earth} \end{pmatrix} = \begin{pmatrix} 1 \\ 1 \\ 1 \end{pmatrix} \tag{5.3.12}$$

for large path lengths and hence the Earth receives roughly an equal number of flavor types [112].

5.4   Discrimination of Neutrino Induced Showers

UHECRs and UHEνs impacting the atmosphere and interacting with atmospheric molecules produce an extended air shower with an electromagnetic component whose development reaches a maximum after traversing a slant depth of about 800 g cm^{-2}. This electromagnetic component gradually becomes extinguished after roughly traveling another 1000 g cm^{-2}. In Fig.21 it is possible to see this slant depth versus zenith angle. This leads to only muons surviving upon reaching the SDs for air showers starting high in the atmosphere (see Fig. 22).

During the first phase of the shower development (*young showers*) where the electromagnetic component is still developing, the time spread of the particles in the shower front is relatively large ($\sim \mu s$). As the shower ages (*old showers*) the time spread between the high energy particles, mostly muons, narrows (~ 100 ns) so that they would all arrive at the SDs within a short window of time. If however, the particle (a neutrino interaction with the atmosphere or a tau decay) interacts deep within the atmosphere the electromagnetic component could reach the ground giving a broad signal in arrival time (see Fig. 23). This signal in each SD is digitized using 40 MHz Flash Analogue Digital Converters which allows the narrow and broad signals to
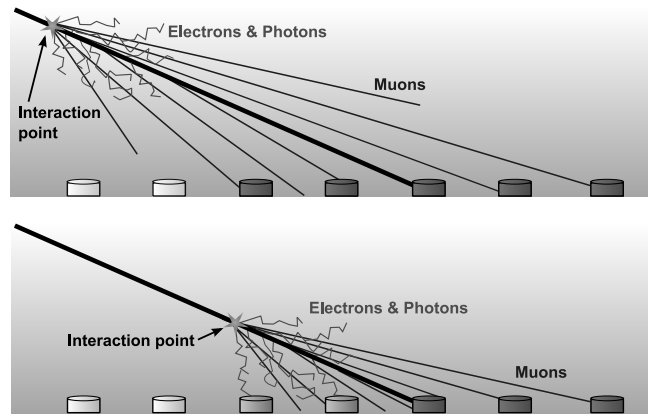
Figure 22 : *Upper panel*: sketch of an inclined shower induced by a hadron interacting high in the atmosphere. The EM component is absorbed and only the muons reach the detector. *Lower panel*: deep inclined shower. Its early region has a significant EM component at the detector level [113].

be distinguished and thus old vs young EAS. Further technical requirements also need to be met to assure that the signal is in fact generated by a neutrino [114].

5.5   Limits of the Diffuse Flux of UHE Tau Neutrinos

For several years the Pierre Auger Collaboration has searched for neutrino signatures in data gathered by the observatory. An earlier report [114] founds n upper limit on the diffuse flux of tau neutrinos from the search of Earth-skimming events in data through 2008 April 30 ($\sim$2 years of exposure with a full SD array). Building on this previous work, to obtain larger statistics, the search was extended to include data until 2010 May 31 ($\sim$3.5 years of exposure with a full SD array). From this larger data set an improved limit was obtained [115].

A relatively small portion of this previously recorded data, from November 1, 2004 to December 31, 2004 (less than 1% of the sample data used in this study), was used in order to optimize the neutrino selection criteria by comparing real measured events to those produced by simulations [114].

Using real data, instead of purely simulations, takes into account all possible detector effects and the normal fluctuations that happen between showers, which make up the overall background to UHEνs which may not be replicated well within Monte Carlo simulations. A training sample established the neutrino selection that was applied to "blind search sample" of data that was collected from January 1, 2004 to May 31, 2010. This sample excluded the data that was collected between November 1, 2004 and December 31, 2004. Accounting for construction of the SD array as well as individual station down times the blind search sample is tantamount to $\sim$ 3.5 years of data collected by the SD array working at full capacity, Fig. 24. The specific details on the selection criteria can be found in Ref. [114].

The blind search did not yield any neutrino candidates. However, assuming a differential spectrum of

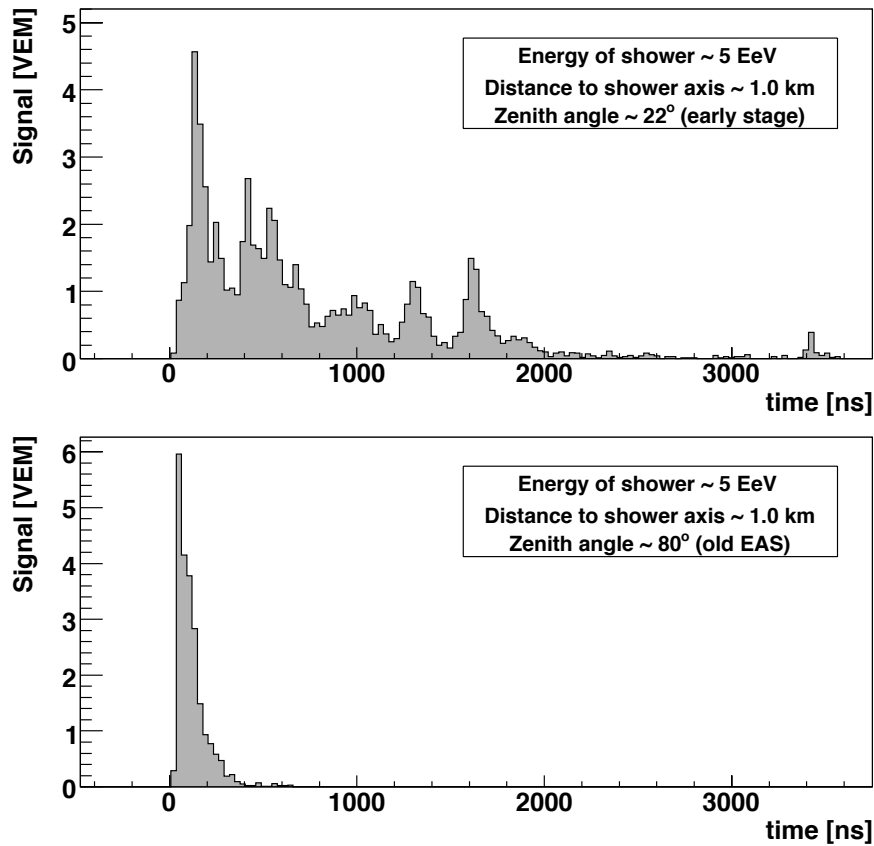$$\Phi(E_\nu) = dN_\nu/dE_\nu = k \cdot E_\nu^{-2} \tag{5.5.1}$$

Figure 23 : FADC traces of stations at 1 km from the shower core for two real showers of 5 EeV. Top panel: early stages of development ($\theta \sim 22°$); bottom: old extensive air shower ($\theta \sim 80°$) [114].

for the diffuse flux of UHEνs and a zero background [113, 114], a 90% confidence level upper limit on the integrated flux of tau neutrinos can be derived [115]:

$$k < 3.2 \times 10^{-8} \quad \text{GeV cm}^{-2}\,\text{s}^{-1}\,\text{sr}^{-1}. \tag{5.5.2}$$

Using a semi-Bayesian extension [116], of the Feldman-Cousins approach [86] systematic uncertainties in the exposure were taken into account in the upper limit. The horizontal lines in Fig. 25 show the upper limit valid in the energy range 1.6×10^{17} eV $\leq E_\nu \leq 2.0 \times 10^{19}$ eV, where $\approx 90\%$ of neutrino events would be detected for a E_ν^{-2} flux.

The differential form of the 90% confidence level is also shown in Fig. 25 as solid lines, where the limit was calculated independently in each energy bin of a width of 0.5 in $\log_{10} E_\nu$ [119]. In addition to this current work, the integrated and differential limits from the search for downward-going neutrinos [113] at the Pierre Auger Observatory, based on another blind search data set collected from November 1, 2007 until May 31, 2010 which is equal to ~ 2.0 years of exposure with the full SD array, are also shown, together with limits from the IceCube Neutrino Observatory [117] and the ANITA experiment [118].

The shaded area in Fig. 25 represents the possible fluxes for cosmogenic neutrinos expected from assumptions made from the possible evolution of the sources themselves, the galactic and extragalactic transition, and for the composition of UHECR coming from the source [101]. This area corresponds to approximately 0.1 to 0.3 cosmogenic neutrino events from the blind
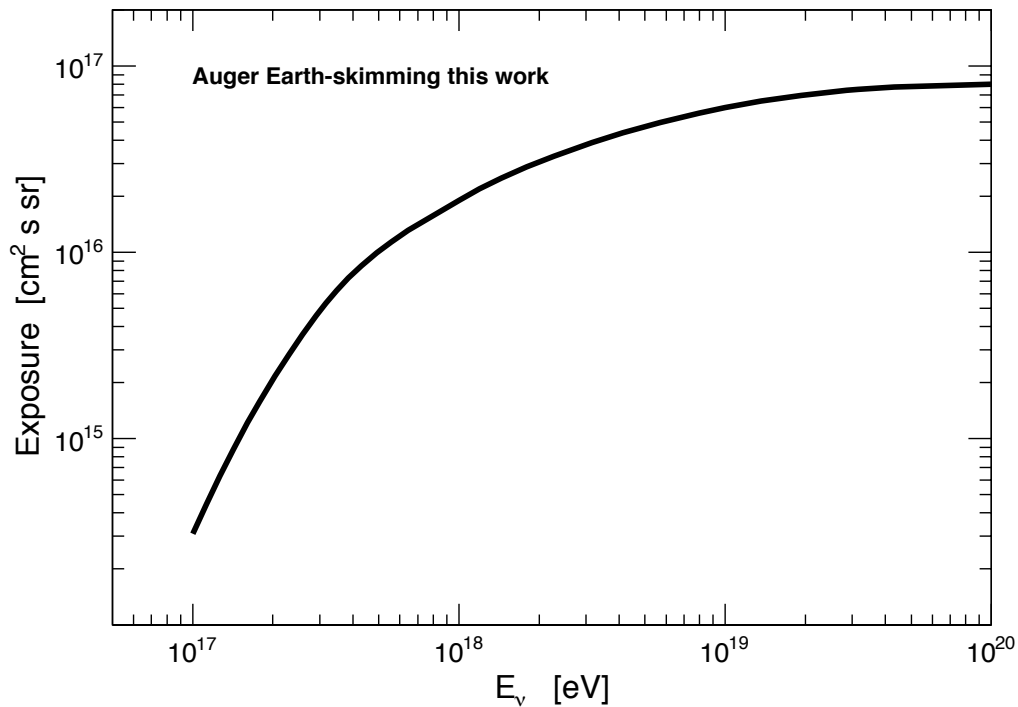
Figure 24 : Exposure of the Surface Detector of the Pierre Auger Observatory for Earth-skimming neutrino initiated showers as a function of the neutrino energy, for data collected between January 1, 2004 and May 31, 2010 [115].

search sample range. Predicted in [102], a diffuse flux of 0.6 cosmogenic neutrino events are expected at the Pierre Auger Observatory with the integrated exposure of the analysis in [115]. This can be compared with the 0.43 events that are expected in the 333.5 days of live-time at the IceCube-40 neutrino telescope [117]. The current cosmogenic neutrino flux bound with energy dependence shown in Fig. 25 and as in [102] is 4 times larger than predicted values. This cosmogenic neutrino flux at 90% confidence level may be excluded with $\sim$10 more years exposure at the Pierre Auger Observatory. It should also be noted that the peak in neutrino flux matches nicely with the maximum sensitivity at the Pierre Auger Observatory, $E_\nu \sim 10^{18}$ eV.

5.6 Sensitivity to Point-Like Sources

In order to search for UHEν events at the Pierre Auger Observatory the search is limited to only highly inclined extended air showers with zenith angles between $90°$ and $96°$ when looking for Earth-skimming (ES) events and between $75°$ and $90°$ when looking at downward-going (DG) events. This restricts neutrino detections to only these zenith angles within specific portions of the sky at any given time. This also means that any point-like sources that hope to be detected must also lie in this range. If a source has a declination, δ, and right ascension α in equatorial coordinates and is seen at the latitude of Pierre Auger, $\lambda = -35.2°$), at a given sidereal time t,
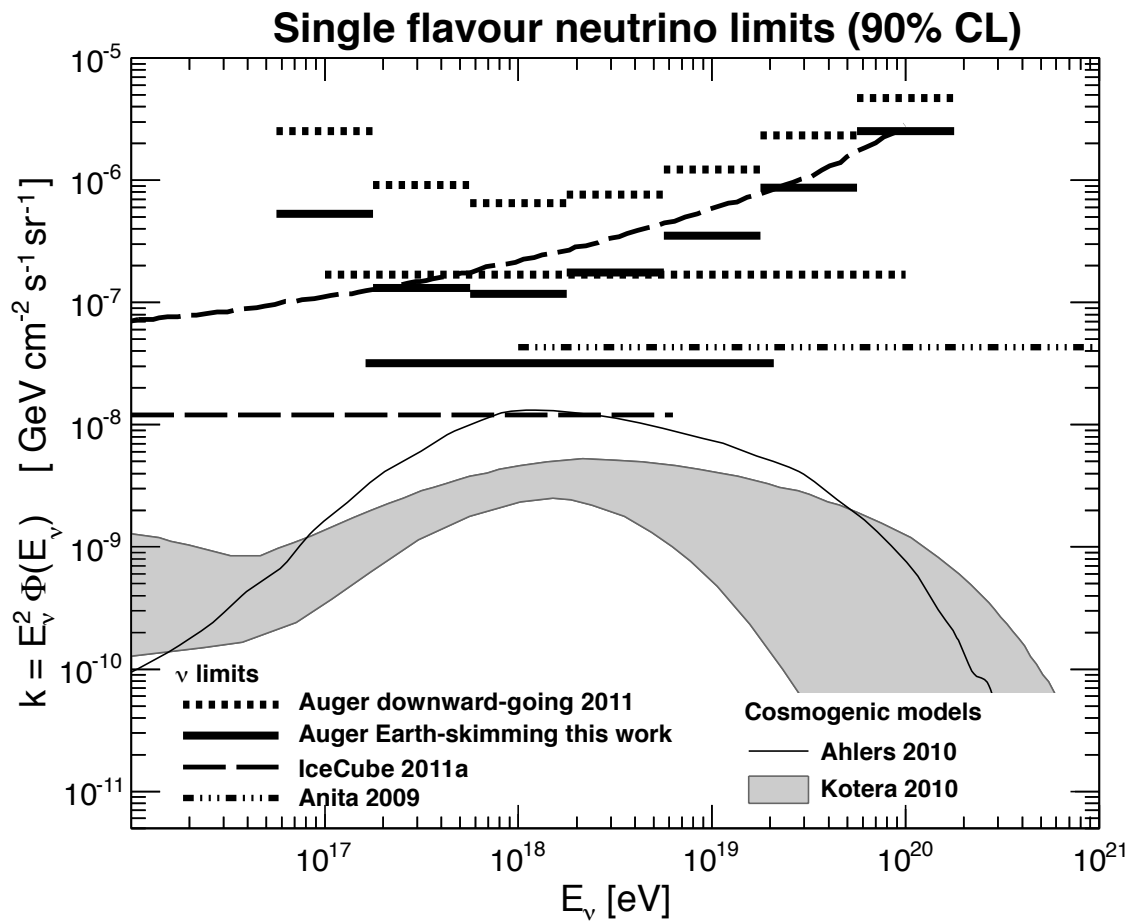
Figure 25 : Differential and integrated upper limits at 90% C.L. on the single flavor E_ν^{-2} neutrino flux from the search for downward-going and Earth-skimming neutrinos at the Pierre Auger Observatory. Integrated upper limits are indicated by horizontal lines, with the corresponding differential limits being represented by segments of width 0.5 in $\log_{10} E_\nu$. Limits from the IceCube Neutrino Observatory [117] and from the ANITA experiment [118] are also shown after proper rescaling to account for single flavor neutrino flux and different energy binning. Predictions for cosmogenic neutrinos under different assumptions [101, 102] are also shown, although predictions almost one order of magnitude lower or higher exist [115].
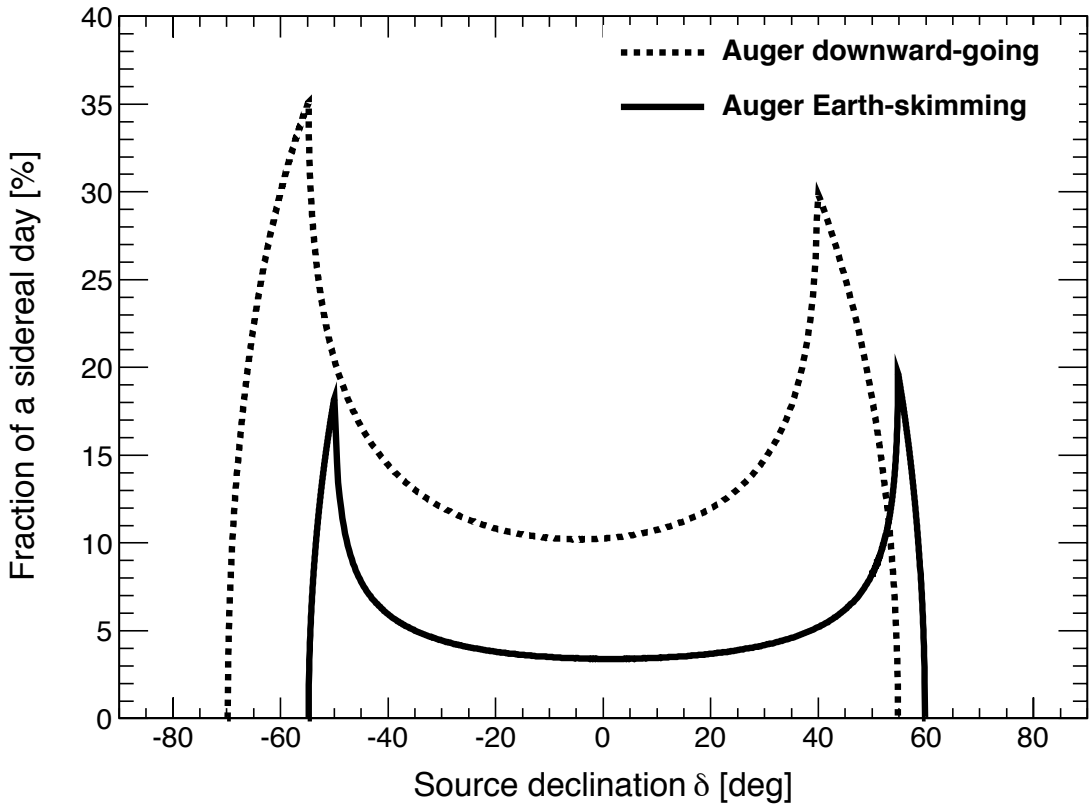
Figure 26 : Fraction of a sidereal day having a point-like source at declination δ detectable by the Pierre Auger Observatory with the Earth-skimming and downward-going neutrino selection. The peaks in are a consequence of the relatively smaller rate of variation of zenith angle with time for directions near the edges of the range accessible to this analysis [115].

then the zenith angle $\theta(t)$ can be found by:

$$\cos\theta(t) = \sin\lambda\,\sin\delta + \cos\lambda\,\cos\delta\,\sin(2\pi t/T - \alpha) \; , \qquad (5.6.1)$$

where T is the duration of one sidereal day. Restricting the zenith angles, $\theta(t)$, in Eq. 5.6.1 to what is detectable via ES and DG analysis Fig shows that the fraction of a sidereal day which a source is detectable is only dependent on the declination. Spanning north to $\delta \sim -65°$ and south to $\delta \sim 55°$ but excluding the regions close to the Northern and Southern Terrestrial Poles, $\delta = 90°$ and $\delta = -90°$ receptively, the Pierre Auger Observatory is sensitive to point-like sources of neutrinos. As an illustration, Centaurus A (an active radio galaxy at $\delta \sim -43°$), is able to be observed $\sim 7\%$ and $\sim 15\%$ for one sidereal day for ES and DG searches.

Using the procedure developed in [113, 114], with the exception of the solid angle integration over the sky, the exposure of the SD as a function of the neutrino energy and the position of the source in the sky, $\mathcal{E}(E_\nu, \delta)$, was evaluated by folding the SD aperture with the neutrino interaction probability and the selection efficiency for each neutrino channel [115]. This integration over the blind search took into account the construction phase of the SD array and individual station dead times giving the exposure for the DG analysis, which is analogous to the

ES analysis, as

$$\mathcal{E}(E_\nu, \delta) = \frac{1}{m} \sum_i \left[\omega_i \, \sigma_i(E_\nu) \int \int \int \cos\theta(t) \, \varepsilon_i(\vec{r}, E_\nu, \theta(t), D, t) \, \mathrm{d}A \, \mathrm{d}D \, \mathrm{d}t \right] \quad (5.6.2)$$

where the integration is done over the SD area A, the neutrino interaction depth D, and the search period t. In Eq. 5.6.2, m is the mass of a nucleon, $\sigma_i(E_\nu)$ is the neutrino-nucleon cross-section [120, 121], and ε_i is the neutrino selection efficiency. The sum runs over the three neutrino flavors with $\omega_i = 1$, corresponding to a 1:1:1 flavor ratio (see subsection 5.3) and over the charged and neutral neutrino current interactions. ε is also dependent on the shower core's point of impact $\vec{r}$, the neutrino interaction depth D, and its energy and zenith angle, and time; all of which have been taken into account in Eq. 5.6.2. From Eq. 5.6.1 we can get the dependence of the exposure due to the source declination $\theta(t)$. Only then, when the source is within the zenith angle range of neutrino selection, are periods considered for the integration over time.

With Eq. 5.6.2 come some systematic uncertainties. Some of the systematic uncertainties have to do with changes in the detector configuration during the data taking, the finite resolution of the SD array, the topography of Pierre Auger itself, and of course simulations of the actual EAS produced by neutrinos interacting with the atmosphere.

5.7   Limits on the Flux of UHEνs From Point-Like Sources

For a point-like source of declination δ the expected number of neutrino events within the energy range $[E_{\min}, E_{\max}]$ can be given as,

$$N_{\text{expected}}^{\text{point source}}(\delta) = \int_{E_{\min}}^{E_{\max}} F(E_\nu) \, \mathcal{E}(E_\nu, \delta) \, \mathrm{d}E_\nu \ , \quad (5.7.1)$$

$F(E_\nu)$ represents the flux of UHEνs from the source. Using the ES and DG analyses no candidate events were selected and also using the conservative assumption of zero background the 90% confidence level was derived. The upper limit was set using 1:1:1 neutrino flavor ratios (see subsection 5.3) and by assuming a differential flux $F(E_\nu) = k_{PS}(\delta) \cdot E_\nu^{-2}$.

The 90% confidence level upper limits on k_{PS} as derived from ES and DG analyses are shown as a function of the source's declination in Fig. 27. Using a broad range of declinations from searches of ES and DG neutrinos limits for k_{PS} at the level of $\approx 5 \times 10^{-7}$ and 2.5×10^{-6} GeV cm^{-2} s^{-1} were acquired respectively. The neutrino energy range to produce this upper limit was in the range of 1.6×10^{17} eV $- 2.0 \times 10^{19}$ eV for the ES analysis, and 1×10^{17} eV $- 1 \times 10^{20}$ eV for the DG analysis, with a negligible dependence of these energy intervals on the source declination. The shape of the upper limits in Fig. 27 is mostly dependent on the time the source was within view of the analysis [115].

Other observatories have also begun the search for UHEνs from point-like sources, namely the IceCube Neutrino Observatory [122] and the Antares Neutrino Telescope [123]. The upper limit bounds obtained by these two experiments apply to energies below that of the Pierre Auger range [115].

Fig. 28 shows the limits for the example used earlier, the radio active galaxy Centaurus A, which is of interest because it is a potential source of UHECRs. In the figure are also constraints
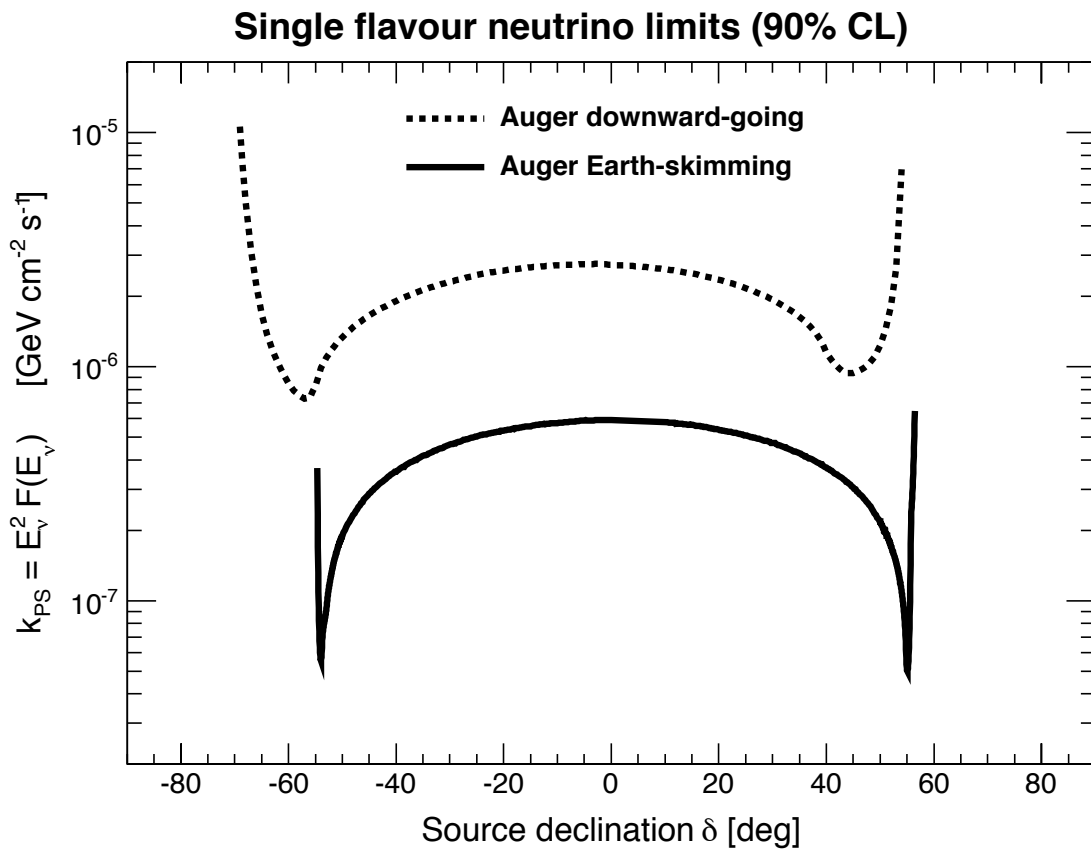
Figure 27 : Upper limits at 90% C.L. on a single flavor E_ν^{-2} flux from a specific point-like source as a function of the source declination. The bounds from the Earth-skimming and downward-going neutrino analyses hold for a neutrino energy range $10^{17} - 10^{20}$ eV (see text for details) [115].

Centaurus A - Single flavour neutrino limits (90% CL)
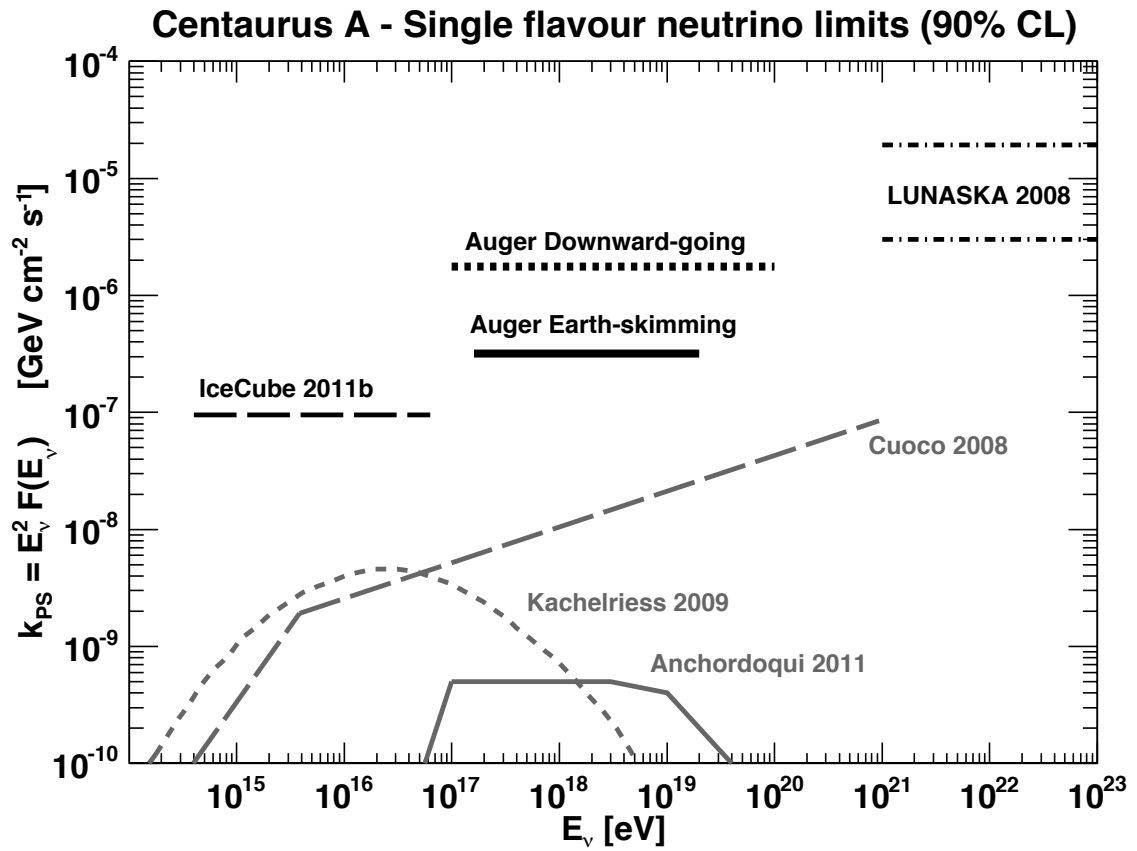
Figure 28 : Upper limits at 90% C.L. on a single flavour E_ν^{-2} flux from the active galaxy Centaurus A from the Earth-skimming and downward-going neutrino analyses, together with bounds from the IceCube Neutrino Observatory [122] and LUNASKA [124]. The predictions for three models of UHEν production – in the jets [125], in the radio-lobes [20], and close to the core of Centaurus A [126] – are also shown.

from other experiments and the predicted fluxes from three theoretical models of UHEν production in the jets [125], in the radio-lobes [20], and close to the core [126]. The number of events expected in our blind search for a flux like in [125] is about 0.1 and 0.02 for the ES and DG selection respectively, the expected number for [126] being one order of magnitude smaller [115].

Chapter 6

Conclusions

Three UHECR species have been examined to search for both large-scale and point-like anisotropic features within their distributed arrival directions using data collected with the Pierre Auger Observatory.

In Chapter 3, we searched for large scale anisotropies in the distribution of arrival directions of cosmic rays detected above 10^{18} eV at the Pierre Auger Observatory. For the first time, these large scale anisotropy searches were performed as a function of both the right ascension and the declination and expressed in terms of dipole and quadrupole moments. Within the systematic uncertainties, no significant deviation from isotropy was revealed. Upper limits on dipole and quadrupole amplitudes were derived under the hypothesis that any cosmic ray anisotropy is dominated by such moments in this energy range. These upper limits provide constraints on the production of cosmic rays above 10^{18} eV, since they allow us to challenge an origin from stationary galactic sources densely distributed in the galactic disk and emitting predominantly light particles in all directions.

In Chapter 4, we showed that the Pierre Auger Observatory has good sensitivity to identify a discrete Galactic source of neutrons if it has a charged particle energy spectrum $\propto E^{-2}$, and interactions of those particles are responsible for it being detectable in TeV γ rays. Our blind search for a flux of neutrons using the Auger data set finds no candidate point on the sky that stands out among the large number of trial targets. Upper limits have been calculated for all parts of the sky using four different energy ranges. Three of those ranges are independent data sets and the fourth is the combination of the other three. The upper limits are generally more stringent where the directional exposure is relatively high, but they are strong enough to be of considerable astrophysical interest in all parts of the exposed sky. Above 1 EeV, the typical (median) flux upper limit is 0.0114 neutron/km^2 yr. This corresponds to an energy flux limit of 0.083 eV/cm^{2}s (or 0.026 EeV/km^{2}yr) in the EeV energy decade if the differential neutron spectrum $\propto E^{-2}$. Even for the regions of minimum sensitivity, the flux upper limit does not exceed 0.046 particles/km^2 yr, corresponding to 0.34 eV/cm^2 s (or 0.106 EeV/km^2 yr) for a spectrum $\propto E^{-2}$.

In Chapter 5, we searched for astrophysical sources of ultrahigh energy neutrinos. The neutrino detection technique is based on the observation of extensive air showers induced by

downward-going neutrinos of all flavours as they interact with the atmosphere, and by upward-going tau neutrinos through the Earth-skimming mechanism. These neutrino-induced showers display characteristic features that allow us their identification in the overwhelming background of regular UHE hadronic showers. At ground level, high zenith angle neutrino events would have a significant electromagnetic component leading to a broad time structure of detected signals in the surface detector array, in contrast to baryonic-induced showers. We have shown that, using Monte Carlo simulations and training data samples, identification criteria for UHE neutrinos can be defined and used to perform a blind search on the remaining data sample. The analysis of the collected data at the Pierre Auger Observatory until 31 May 2010 reveals no candidate events for either downward-going or Earth-skimming neutrinos. Based on this negative result, stringent limits have been placed on the diffuse flux of UHE neutrinos. The absence of candidates in the searches for diffuse neutrino fluxes allowed us to also place restrictive limits on the neutrino fluxes coming from point sources in the field of view of the Pierre Auger Observatory.

It seems that, although extremely large, current observatories are not large enough to study EECRs with the necessary statistics. To deeply explore this new face of the cosmos EECR, facilities need to observe the full sky and must reach colossal exposures, $\mathcal{O}(10^6 \ \mathrm{km}^2 \, \mathrm{sr} \, \mathrm{yr})$. Space-based observatories will be a critical element in accomplishing this endeavor. In this direction, the Extreme Universe Space Observatory (EUSO) attached to the Japanese Experiment Module (JEM) on board the International Space Station (ISS) will provide a breakthrough towards the understanding of astrophysical and physical aspects of the universe at extremely high energies [127]. JEM-EUSO will observe over 4×10^4 km^2 sr yr at E_{GZK}, reaching 100% exposure around 10^{20} eV, where it will observe 6×10^4 km^2 sr yr annually [128], a factor of 10 above Auger.

Bibliography

[1] V. F. Hess, Phys. Z. **13**, 1804 (1912).

[2] L. Anchordoqui, T. C. Paul, S. Reucroft and J. Swain, Int. J. Mod. Phys. A **18**, 2229 (2003) [arXiv:hep-ph/0206072].

[3] W. Bothe, Z. Phys., **59**:1–5 (1929).

[4] H. Geiger, and W. Müller, Die Naturwissenschaften, **31**:617–618. (1928)

[5] B. Rossi, Naure, **125**:636 (1930).

[6] P. Auger, R. Maze, T. Grivet-Meyer, Comptes Rendus **206**, 1721 (1938).

[7] P. Auger, P. Ehrenfest, R. Maze, J. Daudin, Robley, and A. Fréon, Rev. Mod. Phys. **11**, 288 (1939).

[8] W. B. Fretter, Proceedings of Echo Lake Cosmic Ray Symposium (1949).

[9] K. -H. Kampert, A. A. Watson and A. A. Watson, Eur. Phys. J. H **37**, 359 (2012) [arXiv:1207.4827 [physics.hist-ph]].

[10] T. K. Gaisser, Cambridge, UK: Univ. Pr. (1990) page 279

[11] L. Anchordoqui, M. T. Dova, A. G. Mariazzi, T. McCauley, T. C. Paul, S. Reucroft and J. Swain, Annals Phys. **314**, 145 (2004) [hep-ph/0407020].

[12] C. Amsler *et al.* [Particle Data Group], Phys. Lett. B **667**, 1 (2008).

[13] M. Aglietta *et al.* [EAS-TOP Collaboration], Astropart. Phys. **21**, 583 (2004).

[14] T. Antoni *et al.* [KASCADE Collaboration], Astropart. Phys. **24**, 1 (2005) [arXiv:astro-ph/0505413].

[15] W. D. Apel *et al* [KASCADE Collaboration], Astropart. Phys. **31**, 86 (2009) [arXiv:0812.0322 [astro-ph]].

[16] G. Cocconi, Astropart. Phys. **4**, 281 (1996).

[17] K. Greisen, Phys. Rev. Lett. **16**, 748 (1966).

[18] G. T. Zatsepin and V. A. Kuzmin, JETP Lett. **4**, 78 (1966) [Pisma Zh. Eksp. Teor. Fiz. **4**, 114 (1966)].

[19] A. A. Penzias and R. W. Wilson, Astrophys. J. **142**, 419 (1965).

[20] L. A. Anchordoqui, arXiv:1104.0509 [hep-ph].

[21] J. Abraham *et al.* [Pierre Auger Collaboration], Nucl. Instrum. Meth. A **613**, 29 (2010) [arXiv:1111.6764 [astro-ph.IM]].

[22] Y. Tsunesada *et al.* [Telescope Array Collaboration], in Proceeding of the 32nd International Cosmic Ray Conference, Beijing, (ICRC 2011). arXiv:1111.2507 [astro-ph.HE].

[23] E. Fermi, Phys. Rev. **75**, 1169 (1949).

[24] A. M. Hillas, Ann. Rev. Astron. Astrophys. **22**, 425 (1984).

[25] M. Ahlers, L. A. Anchordoqui, J. K. Becker, T. K. Gaisser, F. Halzen, D. Hooper, S. R. Klein. P. Mészáros, S. Razzaque, and S. Sarkar, FERMILAB-FN-0847-A, YITP-SB-10-01.

[26] L. A. Anchordoqui, G. E. Romero and J. A. Combi, Phys. Rev. D **60**, 103001 (1999) [arXiv:astro-ph/9903145].

[27] D. F. Torres and L. A. Anchordoqui, Rept. Prog. Phys. **67**, 1663 (2004) [astro-ph/0402371].

[28] J. Abraham *et al.* [Pierre Auger Collaboration], Astropart. Phys. **27**, 155 (2007) [astro-ph/0606619].

[29] J. Abraham *et al.* [Pierre Auger Collaboration], Astropart. Phys. **29**, 243 (2008) [arXiv:0712.1147 [astro-ph]].

[30] J. Abraham *et al.* [Pierre Auger Collaboration], Astropart. Phys. **31**, 399 (2009) [arXiv:0903.1127 [astro-ph.HE]].

[31] M. Boratav, J. W. Cronin and A. A. Watson, Amsterdam, Netherlands: North-Holland (1992) 234 p. (Nucl. Phys. B, Proc. Suppl. 288 (1992))

[32] J. W. Cronin, In *Snowmass 1994, Particle and nuclear astrophysics and cosmology in the next millennium* 352-357

[33] I. Allekotte *et al.* [Pierre Auger Collaboration], J. Phys. G **28**, 1499 (2002).

[34] J. Abraham *et al.* [Pierre Auger Collaboration], Nucl. Instrum. Meth. A **620**, 227 (2010) [arXiv:0907.4282 [astro-ph.IM]].

[35] R. M. Baltrusaitis *et al.*, Nucl. Instrum. Meth. A **240**, 410 (1985).

[36] T. Abu-Zayyad *et al.*, Nucl. Instrum. Meth. A **450**, 253 (2000).

[37] J. Abraham *et al.* [Pierre Auger Collaboration], Nucl. Instrum. Meth. A **523**, 50 (2004).

[38] I. Allekotte *et al.* [Pierre Auger Collaboration], Nucl. Instrum. Meth. A **586**, 409 (2008) [arXiv:0712.2832 [astro-ph]].

[39] C. Bonifazi [Pierre Auger Collaboration], Nucl. Phys. Proc. Suppl. **190**, 20 (2009) [arXiv:0901.3138 [astro-ph.HE]].

[40] P. Abreu *et al.* [Pierre Auger Observatory Collaboration], Astrophys. J. **760**, 148 (2012) [arXiv:1211.4901 [astro-ph.HE]].

[41] J. Abraham *et al.* [Pierre Auger Collaboration], Phys. Rev. Lett. **101**, 061101 (2008) [arXiv:0806.4302 [astro-ph]].

[42] P. Abreu *et al.* [Pierre Auger Collaboration], arXiv:1107.4809 [astro-ph.HE].

[43] R. U. Abbasi *et al.* [HiRes Collaboration], Phys. Rev. Lett. **100**, 101101 (2008) [arXiv:astro-ph/0703099].

[44] J. Abraham *et al.* [Pierre Auger Collaboration], Phys. Lett. B **685**, 239 (2010) [arXiv:1002.1975 [astro-ph.HE]].

[45] R. Aloisio, V. Berezinsky and A. Gazizov, Astropart. Phys. **34**, 620 (2011) [arXiv:0907.5194 [astro-ph.HE]].

[46] J. Abraham *et al.* [Pierre Auger Collaboration], Phys. Rev. Lett. **104**, 091101 (2010) [arXiv:1002.0699 [astro-ph.HE]].

[47] R. U. Abbasi *et al.* [HiRes Collaboration], Phys. Rev. Lett. **104**, 161101 (2010) [arXiv:0910.4184 [astro-ph.HE]].

[48] M. Ahlers, L. A. Anchordoqui and A. M. Taylor, Phys. Rev. D **87**, 023004 (2013) [arXiv:1209.5427 [astro-ph.HE]].

[49] J. Abraham *et al.* [Pierre Auger Collaboration], Science **318**, 938 (2007) [arXiv:0711.2256 [astro-ph]].

[50] J. Abraham *et al.* [Pierre Auger Collaboration], Astropart. Phys. **29**, 188 (2008) [Erratum-ibid. **30**, 45 (2008)] [arXiv:0712.2843 [astro-ph]].

[51] P. Abreu *et al.* [Pierre Auger Collaboration], Astropart. Phys. **34**, 314 (2010) [arXiv:1009.1855 [astro-ph.HE]].

[52] M. A. Lawrence, R. J. O. Reid and A. A. Watson, J. Phys. G **17**, 733 (1991)

[53] M. Nagano *et al.*, J. Phys. G **18**, 423 (1992).

[54] D. J. Bird *et al.* [HIRES Collaboration], Phys. Rev. Lett. **71**, 3401 (1993).

[55] J. Linsley, Proceedings of ICRC 1963, Jaipur, India, (Commercial Printing Press, Ltd., Bombay, India, 1964), pp. 77-99.

[56] C. T. Hill and D. N. Schramm, Phys. Rev. D **31**, 564 (1985).

[57] J. Candia, S. Mollerach and E. Roulet, JCAP **0305**, 003 (2003) [astro-ph/0302082].

[58] G. Giacinti, M. Kachelriess, D. V. Semikoz and G. Sigl, JCAP **1207**, 031 (2012) [arXiv:1112.5599 [astro-ph.HE]].

[59] A. Calvez, A. Kusenko and S. Nagataki, Phys. Rev. Lett. **105**, 091101 (2010) [arXiv:1004.2535 [astro-ph.HE]].

[60] M. Pohl and D. Eichler, Astrophys. J. **742**, 114 (2011) [arXiv:1108.2135 [astro-ph.HE]].

[61] G. R. Blumenthal, Phys. Rev. D **1**, 1596 (1970).

[62] V. Berezinsky, A. Z. Gazizov and S. I. Grigorieva, Phys. Rev. D **74**, 043005 (2006) [hep-ph/0204357].

[63] V. S. Berezinsky, S. I. Grigorieva and B. I. Hnatyk, Astropart. Phys. **21**, 617 (2004) [astro-ph/0403477].

[64] D. Harari, S. Mollerach and E. Roulet, JCAP **1011**, 033 (2010) [arXiv:1009.5891 [astro-ph.HE]].

[65] P. Abreu *et al.* [Pierre Auger Collaboration], Astropart. Phys. **34**, 627 (2011) [arXiv:1103.2721 [astro-ph.HE]].

[66] J. Abraham *et al.* [Pierre Auger Collaboration], Astropart. Phys. **32**, 89 (2009) [Erratum-ibid. **33**, 65 (2010)] [arXiv:0906.5497 [astro-ph.IM]].

[67] P. Abreu *et al.* [Pierre Auger Collaboration], Astrophys. J. Suppl. **203**, 34 (2012) [arXiv:1210.3736 [astro-ph.HE]].

[68] P. Abreu *et al.* [Pierre Auger Collaboration], ApJL, 762, L **13** (2012) [arXiv:1212.3083 [astro-ph.HE]].

[69] P. Sommers, Astropart. Phys. **14**, 271 (2001) [astro-ph/0004016].

[70] L. A. Anchordoqui, C. Hojvat, T. P. McCauley, T. C. Paul, S. Reucroft, J. D. Swain and A. Widom, Phys. Rev. D **68**, 083004 (2003) [astro-ph/0305158].

[71] P. Billoir and O. Deligny, JCAP **0802**, 009 (2008) [arXiv:0710.2290 [astro-ph]].

[72] R. Beck, Space Sci. Rev. **99**, 243 (2001) [astro-ph/0012402].

[73] M. S. Pshirkov, P. G. Tinyakov, P. P. Kronberg and K. J. Newton-McGee, Astrophys. J. **738**, 192 (2011) [arXiv:1103.0814 [astro-ph.GA]].

[74] C. C. H. Jui [Fly's Eye Collaboration], AIP Conf. Proc. **1367**, 7 (2011).

[75] M. Kachelriess and P. D. Serpico, Phys. Lett. B **640**, 225 (2006) [astro-ph/0605462].

[76] G. L. Cassiday *et al.*, Phys. Rev. Lett. **62**, 383 (1989).

[77] M. Teshima *et al.*, Phys. Rev. Lett. **64**, 1628 (1990).

[78] L. A. Anchordoqui, H. Goldberg, F. Halzen and T. J. Weiler, Phys. Lett. B **593**, 42 (2004) [astro-ph/0311002].

[79] L. A. Anchordoqui, H. Goldberg and T. J. Weiler, Phys. Rev. Lett. **87**, 081101 (2001) [astro-ph/0103043].

[80] L. A. Anchordoqui, H. Goldberg and T. J. Weiler, Phys. Rev. D **84**, 067301 (2011) [arXiv:1103.0536 [astro-ph.HE]].

[81] L. A. Anchordoqui, Acta Phys. Polon. B **36**, 495 (2005) [astro-ph/0410087].

[82] L. A. Anchordoqui, J. F. Beacom, H. Goldberg, S. Palomares-Ruiz and T. J. Weiler, Phys. Rev. Lett. **98**, 121101 (2007) [astro-ph/0611580].

[83] J. Beringer *et al.* [Particle Data Group Collaboration], Phys. Rev. D **86**, 010001 (2012).

[84] J. A. Hinton and W. Hofmann, Ann. Rev. Astron. Astrophys. **47**, 523 (2009) [arXiv:1006.5210 [astro-ph.HE]].

[85] T. -P. Li and Y. -Q. Ma, Astrophys. J. **272**, 317 (1983).

[86] G. J. Feldman and R. D. Cousins, Phys. Rev. D **57**, 3873 (1998) [physics/9711021 [physics.data-an]].

[87] G. Zech, Nucl. Instrum. Meth. A **277**, 608 (1989).

[88] K. M. Gorski, E. Hivon, A. J. Banday, B. D. Wandelt, F. K. Hansen, M. Reinecke and M. Bartelman, Astrophys. J. **622**, 759 (2005) [astro-ph/0409513].

[89] T. K. Gaisser, F. Halzen and T. Stanev, Phys. Rept. **258**, 173 (1995) [Erratum-ibid. **271**, 355 (1996)] [hep-ph/9410384].

[90] F. Halzen and D. Hooper, Rept. Prog. Phys. **65**, 1025 (2002) [astro-ph/0204527].

[91] L. Anchordoqui and F. Halzen, Annals Phys. **321**, 2660 (2006) [hep-ph/0510389].

[92] J. K. Becker, Phys. Rept. **458**, 173 (2008) [arXiv:0710.1557 [astro-ph]].

[93] L. A. Anchordoqui and T. Montaruli, Ann. Rev. Nucl. Part. Sci. **60**, 129 (2010) [arXiv:0912.1035 [astro-ph.HE]].

[94] V. S. Beresinsky and G. T. Zatsepin, Phys. Lett. B **28**, 423 (1969).

[95] F. W. Stecker, Astrophys. J. **228**, 919 (1979).

[96] S. Yoshida and M. Teshima, Prog. Theor. Phys. **89**, 833 (1993).

[97] R. J. Protheroe and P. A. Johnson, Astropart. Phys. **4**, 253 (1996) [arXiv:astro-ph/9506119].

[98] R. Engel, D. Seckel and T. Stanev, Phys. Rev. D **64**, 093010 (2001) [arXiv:astro-ph/0101216].

[99] Z. Fodor, S. D. Katz, A. Ringwald and H. Tu, JCAP **0311**, 015 (2003) [arXiv:hep-ph/0309171].

[100] L. A. Anchordoqui, H. Goldberg, D. Hooper, S. Sarkar and A. M. Taylor, Pierre Auger Observatory," Phys. Rev. D **76**, 123008 (2007) [arXiv:0709.0734 [astro-ph]].

[101] K. Kotera, D. Allard and A. V. Olinto, JCAP **1010**, 013 (2010) [arXiv:1009.1382 [astro-ph.HE]].

[102] M. Ahlers and F. Halzen, [arXiv:1208.4181 [astro-ph.HE]].

[103] D. Hooper, A. Taylor and S. Sarkar, Astropart. Phys. **23**, 11 (2005) [arXiv:astro-ph/0407618].

[104] M. Ave, N. Busca, A. V. Olinto, A. A. Watson and T. Yamamoto, Astropart. Phys. **23**, 19 (2005) [arXiv:astro-ph/0409316].

[105] J. Alvarez-Muniz and F. Halzen, Astrophys. J. **576**, L33 (2002) [astro-ph/0205408].

[106] L. A. Anchordoqui, H. Goldberg, F. Halzen and T. J. Weiler, Phys. Lett. B **600**, 202 (2004) [astro-ph/0404387].

[107] K. S. Capelle, J. W. Cronin, G. Parente and E. Zas, Astropart. Phys. **8**, 321 (1998) [astro-ph/9801313].

[108] J. Abraham *et al.* [Pierre Auger Collaboration], Phys. Rev. Lett. **100**, 211101 (2008) [arXiv:0712.1909 [astro-ph]].

[109] M. C. Gonzalez-Garcia and Y. Nir, Rev. Mod. Phys. **75**, 345 (2003) [hep-ph/0202058].

[110] M. C. Gonzalez-Garcia and M. Maltoni, Phys. Rept. **460**, 1 (2008) [arXiv:0704.1800 [hep-ph]].

[111] M. C. Gonzalez-Garcia, M. Maltoni and J. Salvado, JHEP **1004**, 056 (2010) [arXiv:1001.4524 [hep-ph]].

[112] J. G. Learned and S. Pakvasa, Astropart. Phys. **3**, 267 (1995) [hep-ph/9405296, hep-ph/9408296].

[113] P. Abreu *et al.* [Pierre Auger Collaboration], Adv. High Energy Phys. **2013**, 708680 (2013) [arXiv:1304.1630 [astro-ph.HE]].

[114] J. Abraham *et al.* [Pierre Auger Collaboration], Phys. Rev. D **79**, 102001 (2009) [arXiv:0903.3385 [astro-ph.HE]].

[115] P. Abreu *et al.* [Pierre Auger Collaboration], Astrophys. J. **755**, L4 (2012) [arXiv:1210.3143 [astro-ph.HE]].

[116] J. Ahrens *et al.* [AMANDA Collaboration], Phys. Rev. D **67**, 012003 (2003) [astro-ph/0206487].

[117] R. Abbasi *et al.* [IceCube Collaboration], Phys. Rev. D **83**, 092003 (2011) [Erratum-ibid. D **84**, 079902 (2011)] [arXiv:1103.4250 [astro-ph.CO]].

[118] P. W. Gorham *et al.* [ANITA Collaboration], Phys. Rev. D **85**, 049901 (2012) [arXiv:1011.5004 [astro-ph.HE], arXiv:1003.2961 [astro-ph.HE]].

[119] L. A. Anchordoqui, J. L. Feng, H. Goldberg and A. D. Shapere, Phys. Rev. D **66**, 103002 (2002) [hep-ph/0207139].

[120] L. A. Anchordoqui, A. M. Cooper-Sarkar, D. Hooper and S. Sarkar, Phys. Rev. D **74**, 043008 (2006) [hep-ph/0605086].

[121] A. Cooper-Sarkar and S. Sarkar, JHEP **0801**, 075 (2008) [arXiv:0710.5303 [hep-ph]].

[122] R. Abbasi *et al.* [IceCube Collaboration], Astrophys. J. **732**, 18 (2011) [arXiv:1012.2137 [astro-ph.HE]].

[123] S. Adrian-Martinez *et al.* [Antares Collaboration], Astrophys. J. **743**, L14 (2011) [arXiv:1108.0292 [astro-ph.HE]].

[124] C. W. James, R. J. Protheroe, R. D. Ekers, J. Alvarez-Muniz, R. A. McFadden, C. J. Phillips, P. Roberts and J. D. Bray, arXiv:0906.3766 [astro-ph.HE].

[125] A. Cuoco and S. Hannestad, Phys. Rev. D **78**, 023007 (2008) [arXiv:0712.1830 [astro-ph]].

[126] M. Kachelriess, S. Ostapchenko and R. Tomas, New J. Phys. **11**, 065017 (2009) [arXiv:0805.2608 [astro-ph]].

[127] J. H. Adams, Jr. *et al.*, arXiv:1203.3451 [astro-ph.IM].

[128] J. H. Adams *et al.* [JEM-EUSO Collaboration], Astropart. Phys. **44**, 76 (2013).

CURRICULUM VITAE

Larry Buroker

EDUCATION

Sep. 2009—Present,   University of Wisconsin-Milwaukee

Bachelor of Science (2009),   University of Wisconsin-Milwaukee

AWARDS

2009-2010   Chancellor Fellowship (UWM)

2008-2009   Stipends for Undergraduate Research Fellows (SURF) (UWM)

2008   Internship Award at the Advanced Analysis Facility (UWM)

PUBLICATIONS

- *Techniques for Measuring Aerosol Attenuation using the Central Laser Facility at the Pierre Auger Observatory*
  L. Buroker with the Pierre Auger Collaboration,
  JINST **8**, P04009 (2013)
  e-Print: arXiv:1303.5576

- *Interpretation of the Depths of Maximum of Extensive Air Showers Measured by the Pierre Auger Observatory*
  L. Buroker with the Pierre Auger Collaboration,
  JCAP **1302**, 026 (2013)
  e-Print: arXiv:1301.6637

- *Results of a self-triggered prototype system for radio-detection of extensive air showers at the Pierre Auger Observatory*
  L. Buroker with the Pierre Auger Collaboration,
  JINST **7**, P11023 (2012)
  e-Print: arXiv:1211.0572

- *Antennas for the Detection of Radio Emission Pulses from Cosmic-Ray*
  L. Buroker with the Pierre Auger Collaboration,
  JINST **7**, P10011 (2012)
  e-Print: arXiv:1209.3840

- *The Rapid Atmospheric Monitoring System of the Pierre Auger Observatory*
  L. Buroker with the Pierre Auger Collaboration,

JINST **7**, P09001 (2012)
e-Print: arXiv:1208.1675

- *Measurement of the Cosmic Ray Energy Spectrum Using Hybrid Events of the Pierre Auger Observatory*
  L. Buroker with the Pierre Auger Collaboration,
  Eur. Phys. J. Plus **127**, 87 (2012)
  e-Print: arXiv:1208.6574

- *Search for point-like sources of ultra-high energy neutrinos at the Pierre Auger Observatory and improved limit on the diffuse flux of tau neutrinos*
  L. Buroker with the Pierre Auger Collaboration,
  Astrophys. J. **755**, L4 (2012)
  e-Print: arXiv:1210.3143

- *A Search for Point Sources of EeV Neutrons*
  L. Buroker with the Pierre Auger Collaboration,
  Astrophys. J. **760**, 148 (2012)
  e-Print: arXiv:1211.4901

- *Constraints on the origin of cosmic rays above 10^{18} eV from large scale anisotropy searches in data of the Pierre Auger Observatory*
  L. Buroker with the Pierre Auger Collaboration,
  Astrophys. J. **762**, L13 (2012)
  e-Print: arXiv:1212.3083

- *Large scale distribution of arrival directions of cosmic rays detected above 10^{18} eV at the Pierre Auger Observatory*
  L. Buroker with the Pierre Auger Collaboration,
  Astrophys. J. Suppl. **203**, 34 (2012)
  e-Print: arXiv:1210.3736

- *Study of Structural, Magnetic and Dielectric Properties of Magnetoelectric $TbMn_{1-x}Cu_xO_3$*
  S.K. Ray, L. Buroker, M. S. Williamsen, Y. Zou, S. Sen, and P. Guptasarma
  Symposium F, Vol. 1199E, Multiferroic and Ferroelectric Materials,
  Materials Research Society (2010)

- *Competing Magnetic Interactions in Magnetoelectric $YbMnO_3$*
  S. K. Ray, Y. Zou, M. S. Williamsen, S. Sen, L. Buroker, and P. Guptasarma
  Vol. 1183: Novel Materials and Devices for Spintronics (ed: O.G. Hei nonen, S. Sanvito, V.A. Dediu, N. Rizzo), Materials Research Society, ISBN: 978-1-60511-156-8 (2009).

PRESENTATIONS

- *Synthesis and Properties of PbTi$_{(1-x)}$Ni$_{(x)}$ O$_3$*
  American Physical Society March Meeting
  Pittsburgh, PA, March 2009.

- *Synthesis and Properties of PbTi$_{(1-x)}$ Ni$_{(x)}$ O$_3$*
  23rd National Conference on Undergraduate Research
  LaCrosse, WI, August 2009.

- *Investigation of the Structural and Magnetic Properties of TbMn$_{(1-x)}$ Cu$_{(}$x$_{)}$ O$_3$ and PbTi$_{(1-x)}$ Ni$_{(x)}$ O$_3$*
  UW-Milwaukee Undergraduate Research Symposium
  Milwaukee, WI, April 2010.